Master's thesis

2022

Håkon Broch

NTNU
Norwegian University of
Science and Technology
Faculty of Information Technology and Electrical
Engineering
Department of Electric Power Engineering

Håkon Broch

Direct Drive PMSM Characteristics for Retrofit in Regional Turboprops Using a Design Space Approach

June 2022

NTNU
Norwegian University of
Science and Technology

NTNU
Norwegian University of
Science and Technology

NTNU

Norwegian University of
Science and Technology

Direct Drive PMSM Characteristics for Retrofit in Regional Turboprops Using a Design Space Approach

Håkon Broch

Energy and Environmental Engineering
Submission date: June 2022
Supervisor: Jonas Kristiansen Nøland
Co-supervisor: Andrea Bocchese

Norwegian University of Science and Technology
Department of Electric Power Engineering

Sammendrag

Et design-rom som dekker effekt- og turtallsbehovet til en representativ samling av turbo-prop fly ønskes generert for å avdekke tendenser i ytelsen til permanentmaskinmotorer uten bruk av giring. Design-rommet utgjør effektytelser mellom 500kW og 4 MW, samt omdreiningshastigheter mellom 800 og 2000 o/min. Dette gjennomføres ved bruk av en analytisk algoritme der spesifikk effekt, spesifikt dreiemoment, og effektivitet brukes som ytelsesindikatorer. Resultatene som genereres analytisk blir deretter verifisert ved numerisk analyse av et utvalg av motorer.

Undersøkelsen viser at spesifikk effekt holdes relativt konstant sammenliknet med flyene i design-rommet, med verdier mellom 2.8 og 3.7 kW/kg. Spesifikt dreiemoment og effektivitet øker begge med motorstørrelse, og ligger henholdsvis i området mellom 18 til 34 Nm/kg og 98 til 98.7 %. Resultatene taler for at det i et effektivitetsøyemed kan være bedre å elektrifisere større turboprop-fly.

Det blir også vist at elektrisk motorvekt øker opp mot 30% i forhold til tilsvarende turbinmotorer, i motsetning til de minste elektriske motorene som kan være opp til 40% lettere enn sine motparter.

Acknowledgements

I would, first of all, acknowledge the guidance and assistance I have received from my supervisors—Jonas Kristiansen Nøland and Andrea Bocchese—and express my gratitude for their time and efforts. I would also thank Runar Mellerud, which has assisted me with work in COMSOL and other questions. I finally want to thank my family, friends, and significant other for their humor and guidance.

Håkon Broch

Trondheim, June 7, 2022

Contents

Direct Drive PMSM Characteristics for Retrofit in Regional Turboprops Using a Design Space Approach

Håkon Broch[1*]; Supervisors: Jonas Kristiansen Nøland[1] and Andrea Bocchese[2]
[1] Department of Electric Power Engineering, Norwegian University of Science and Technology, Trondheim, Norway
[2] Rolls Royce Electrical Norway, Trondheim, Norway
[*]E-mail: hakon@broch.as

***Abstract*—A design space for radial flux direct drive PMSMs is generated across the performance requirements of a representative selection of turboprop aircraft. This equates to power outputs in the range 500 kW–4MW, and rotational speeds in the range 800–2000 rpm. The electric motor designs are generated using an analytical algorithm, and their specific power, specific torque and motor efficiency. These results are then verified by selective FEM simulation to confirm their validity.**

It is found that specific power remains relatively constant in motor designs for turboprop aircraft across the entire performance range, with results in the range between 2.8–3.7 kW/kg. Specific torque and efficiency increases with motor size ranging between 18–34 Nm/kg and 98–98.7%. This indicates that retrofit designs for larger aircraft are more optimal in terms of efficiency, and similar in terms of specific power.

It is also found that larger electric motors are comparatively 30% heavier than their turbine driven counterparts, unlike smaller electric motors that can be up to 40% lighter.

Nomenclature

A. Electromagnetic parameters

$\alpha_b,\ K_{hys},\ K_{eddy},\ K_{an}$	Bertotti loss coefficients	—
$\alpha_s,\ \beta_s,\ k_s$	Steinmetz loss coefficients	—
$\hat{B}$	Peak flux density	T
$\hat{I}$	Current peak	A
μ_r	Magnet relative recoil permeability	—
μ_0	Vacuum magnetic permeability	H/m
ϕ_p	Flux per pole	Wb
ϕ_{p1}	Flux per pole fundamental space component	Wb
ρ	Copper resistivity	Ωm
ρ_0	Copper resistivity coefficient	Ωm
θ_o	Motor current angle offset	rad
B_g	Air gap flux density	T
B_r	Magnet remanence	T
B_{g1}	Air gap flux density fundamental harmonic	T
B_{max}	Maximum allowable flux density	T
B_{sat}	Saturation flux density	T
C	Carter coefficient	—
f_{el}	Electrical frequency	Hz
h'_{ag}	Equivalent air gap height	m
H_c	Magnet coercivity	A/m
$I_a,\ I_b,\ I_c$	Phase currents	A
I_r	Per phase current	A
J	Current density	A/mm^2
J_{max}	Maximum allowable current density	A/mm^2
$K_1,\ K_2,\ K_3,\ K_4$	Electrical dimensioning coefficients	—
K_i	Lamination pack coefficient	—
K_c	Copper temperature coefficient	$1/°C$
K_s	Linear current density	A/m
k_{wdg}	Winding factor	—
l'_m	Equivalent magnet height	m
L_{end}	End winding inductance	H
L_{gap}	Magnetizing inductance	H
L_s	Slot leakage inductance	H
N_{ph}	Number of series conductors per phase	—
p_-	Per mass losses	W/kg
P_{an}	Iron anomalous losses	W
P_{eddy}	Iron eddy current losses	W
P_{hys}	Iron hysteresis losses	W
P_{iron}	Motor iron losses	W
P_{ohmic}	Ohmic losses	W
R_s	Per phase equivalent resistance	Ω
T_{el}	Electrical period	s
V_r	Rated voltage	V
X_s	Per phase equivalent reactance	Ω
z	Winding factor calculation parameter	—

B. General parameters

ω	Angular velocity	rad/s
ρ	Mass density	kg/m^3
n	Revolutions per minute	rpm
r	Radius	m
T	Period	s
t	Time variable	s

C. Geometric parameters

α_m	Magnet width fraction of pole pitch	m
ρ_{cu}	Winding material density	kg/m^3
ρ_{fe}	Iron material density	kg/m^3
ρ_{pm}	Magnet material density	kg/m^3
ρ_{sh}	Shaft material density	kg/m^3
τ_p	Pole pitch	m
τ_s	Slot pitch	m
ξ_{enc}	Enclosure weight fraction of total weight	kg
A_{us}	Slot area	m^2
A_{wire}	Per phase equivalent wire cross section	m^2

June 7, 2022

D_{ag}	Motor diameter at middle of air gap	m
D_{er}	Motor external diameter	m
D_{h1}	Motor diameter to windings	m
D_{min}	Rotor iron inner diameter	m
D_{sh}	Shaft diameter	m
h_{11}	Tooth shoe tip height	m
h_{12}	Tooth shoe taper height	m
h_{ag}	Air gap height	m
h_{us}	Tooth height	m
h_{yr}	Rotor yoke thickness	m
h_{ys}	Stator yoke thickness	m
k_{fill}	Winding fill factor for single winding	—
l_m	Magnet thickness	m
L_{ew}	End winding turn length	m
L_{turn}	Turn length	m
M_{cu}	Winding weight	kg
M_{enc}	Approx. enclosure weight	kg
M_{pm}	Magnet weight	kg
M_{sh}	Shaft weight	kg
M_{tot}	Total motor weight	kg
M_{tth}	Stator teeth weight	kg
M_{yr}	Rotor yoke weight	kg
M_{ys}	Stator back iron weight	kg
N_{seg}	Number of segments in FEM-analysis	—
p	Number of poles	—
q	Number of slots per pole per phase	—
w_m	Magnet width	m
w_o	Tooth spacing	m
w_{sb}	Slot bottom width	m
w_{st}	Slot top width	m
w_{sw}	Tooth shoe width	m
w_{tt}	Tooth width	m
D. Mechanical parameters		
η_p	Ideal propeller efficiency	—
a	Speed of sound	m/s
D_{prop}	Propeller diameter	m
M_{tip}	Relative propeller tip speed	$Mach$
N_r	Rated rotational speed	rpm
n_{approx}	Approximated propeller rpm	rpm
P_r	Rated output power	W
P_{avg}	Average output power	W
T_r	Rated torque	Nm
T_o	Operating temperature	$°C$
V_{as}	Aircraft air speed	m/s
V_{tip}	Propeller tip speed	m/s

I. Introduction

In order to achieve global emission reductions, at least partial electrification of the transportation sector is needed. Electrification in land vehicles and sea vessels is already underway, with each requiring wildly different propulsion architectures and system requirements, and posing different design challenges.

Electrification of civilian aviation is also subject to its unique set of challenges, with particularly weight and energy storage capacity being two considerations being in direct opposition to each other—more so than in other forms of transportation.

Different technologies are examined to fully or partially electrify aviation in order to reach electrification targets, e.g., those set by the European Union [1] or NASA [2]. More-electric aircraft can be said to be the first step in aeronautical electrification and are characterized by electrifying all non-propulsive systems. The next step is hybrid-electric aircraft, where at least some of the propulsive power originates from electric machines, while the last step is fully electrified aircraft.

Both hybrid and fully electric propulsion architectures employ electric drives as their source of mechanical power, which comes with multiple benefits. In addition to having no inherent emissions, electric motors have lower maintenance costs due to their mechanical simplicity, less noise pollution, higher energy efficiency, and are unaffected in performance by altitude [3, 4].

A fully electric aircraft employs only electrical motors in its propulsion system, meaning energy storage is entirely non-fossil, as shown in fig. 1. Currently, energy storage is a major hurdle in the development of partially—or fully—electrified aviation. Battery technology is currently not power-dense enough to compete with fossil energy storage. This has led to different propulsion architectures being proposed to mitigate the issue. The two most common are *series hybrid*, and *parallel hybrid* propulsion.

Hybridization is a popular topic in aeronautical propulsion research and is closer than fully electric propulsion to reaching maturity. Employing a hybrid-electric propulsion system means that energy can be stored by traditional and more technologically mature means. The two most common ways of implementing this topology are in the parallel and series hybrid systems, portrayed in figs. 2 and 3. In series hybrid propulsion, an electric motor supplies all mechanical power to a propeller—like in fully electric aircraft. Parallel hybrid propulsion, however, is characterized by some of the mechanical power being supplied by a turboshaft, meaning any electric drives do not need to supply *all* propulsive power. This, in turn, means they can be reduced in size.

When it comes to electrifying aircraft, most research is focused on short-haul flights. This priority stems from the current limitation in energy storage, making shorter

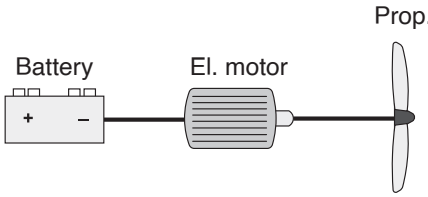

Figure 1: Fully electric propulsion system

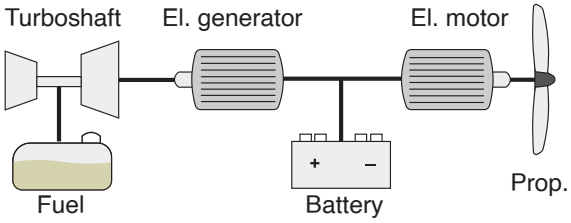

Figure 2: Series hybrid propulsion system

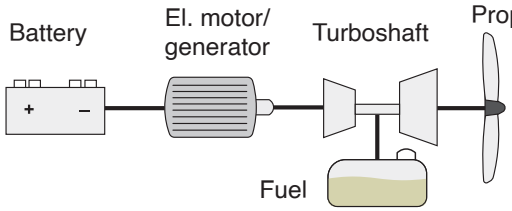

Figure 3: Parallel hybrid propulsion system

routes more viable [5]. These flights are often called regional flights.

Turboprop aircraft is an aircraft type often utilized in regional aviation. Turboprops use turbine-powered propellers, unlike the more common turbofan aircraft, which employ faster-rotating fans. This causes them to have a higher top speed than their turboprop counterparts while making them less efficient [6, 7]. This attribute makes propeller aircraft a more attractive target for electrification.

In order to gain an understanding of electric motors in aircraft, one must begin by understanding the requirements posed by the aircraft that will employ them.

If desired, one can design the aircraft and its motors in parallel, finding ways that the two systems function optimally together and achieve goals set by regulations or customers. This method allows for novel aircraft design concepts, like distributed propulsion, where a few large motors are exchanged for several smaller ones. However, the parallel design of aircraft and motors is a complicated process and demands a broad—cross-disciplinary—scope.

Another approach is investigating contemporary aviation and basing electric motor design on those requirements. The term *retrofit* becomes relevant, as a motor designed based on the requirements of an actual aircraft could, by definition, be exchanged for that aircraft's actual engine.

Retrofitting an airframe with an electric motor often requires retrofitting the entire propulsion system, depending on the degree of electrification. This has already been achieved in experimental aircraft with the Magnix' *eCaravan* [8], Siemens' *Extra 330LE* [9] and to a certain extent Rolls-Royce's *Spirit of Innovation* [10].

Optimizing the design of a complete propulsion system is an active research subject. The main focus is on how stored energy gets converted into power in an electric motor. The next step, of course, is converting the motor mechanical energy into propulsive thrust through a propeller.

The propeller and turbine engine interface has been extensively researched, and propellers can be considered a mature technology. As no high-power electric motor for aircraft currently is in use, the specific interface between current regional aircraft propellers and electric motors is not subject to the same level of maturity. This point is especially true in series, or fully electric aircraft, where electric motors produce all thrust.

There are two methods of connection between a motor and its propeller, either through gearing, or direct drive[1], where the propeller shaft is connected directly to the motor.

With the intent of making electric aircraft motors low weight, some motors are designed to operate at high rotational velocities of 10 000–20 000 rpm [11]. Motors with rotational velocities of this magnitude require gearing if the propellers in conventional aircraft are used.

Despite their intrinsically higher weight, direct-drive electric motors are a relevant alternative to geared drives. Gearing adds mass complexity and mechanical losses to the propulsion system. Because of this, several projects designing direct-drive electric motors exist, like the Magnix Magni 500 and 250 [12], and the Siemens P200D [9].

A. Motivation and Objective

Most aeronautical direct-drive electric motors presented in literature present specific designs for relatively low power use compared to regional aircraft [4, 11, 13, 14], which typically have motors rated from 1–4 MW. The design and performance of direct drive motors with high power rating and specific power for retrofit in existing turboprop aircraft are not examined to the same degree.

This thesis aims to map the design characteristics of direct drive motors with high power ratings and densities based on current aircraft power requirements. This mapping includes identifying the motor performance requirements of modern

[1]Some literature use the term *direct drive*—to indicate the manner of which a propeller is connected to the turbine shaft, regardless of any gearing. This thesis, however, uses the term only to indicate whether or not a gearbox is placed between motor and propeller.

turboprop aircraft and using these as the basis for motor design.

A general impression of motor performance compared to existing aircraft can indicate which types of aircraft are more relevant for electric motor retrofit.

It is also possible to gain knowledge of the performance of the electric motors, as direct drive propulsion in aircraft requires relatively high power and low rpm compared to automotive motors.

Lastly, it may be possible to draw conclusions regarding how future electrical aircraft can be designed based on which motor designs are more viable. This is especially relevant regarding the viability of distributed propulsion.

Mapping of motor performance can be achieved by using a design space approach. A 2-dimensional span of regional aircraft performance demand used as input parameters in a motor design algorithm can allow for a wide span of motor designs.

When motor designs are completed, an examination into how the motors perform during a flight cycle will be made, giving an impression of the viability of these electric motors.

B. Structure

This thesis will begin by going through the basic theory behind propellers and the typical mission profile of a turboprop aircraft, laying the foundation for motor design. An analytical motor design algorithm will be presented as the base method for achieving the rapid computations needed to generate a large number of motor designs. These results will then be verified by numerical simulation of some motors. The simulated motors will also be manually optimized and compared to verify the analytical the ability of the algorithm to generate optimal designs. The resulting data will then be compared to regional turboprop airliner performance to investigate the junction between electric motors and aircraft. Lastly, the optimized motors will have their performance through a typical flight cycle investigated.

This thesis builds on a preceding project report, by the author, with similar research objectives [15]. The previous work includes identifying trends in lightweight electric motors, gathering and compiling aircraft propeller data, and the base methods used to generate analytical results.

II. Theory

This section includes a basic description of propellers and their operational characteristics, an introduction to the equations used when analytically dimensioning motors, as well as an introduction to loss calculation from numerical FEA results.

A. Propeller Dynamics

In order to be able to analyze the interface between a propeller and a motor, it is necessary to present the basic rules that govern propellers for turboprop aircraft. Propellers are limited in rotational speed and have specific operational characteristics relevant when designing motors.

The fundamental relationship between propeller speed, power, and torque—shown in eq. (1)—describes the main parameters linking a propeller and a motor together.

$$T_r = \frac{P_r}{N_r \frac{2\pi}{60}} \tag{1}$$

Near all propellers used by turboprop aircraft are what are called fixed-speed propellers. Their speed remains relatively constant during the entire flight. The highest rpm is reached during take-off and is subsequently reduced during cruise and landing. The Dash 8–Q400—a typical sizeable civilian turboprop aircraft—has a maximum propeller take-off speed of 1020 rpm while typically reducing this to 850 rpm during cruise and landing [16]. The narrow envelope of rotational velocity means that the variation in propulsive thrust must mainly come from a change in propeller torque, which is done by changing the propeller blade pitch.

Propellers that are fixed speed also adjust blade angle to ensure optimal efficiency. The relationship between airspeed (V_{as}) and the resultant airflow from propeller rotation ($\omega \cdot r$) results in a vector representing the actual direction of airflow the propeller blade meets (V_{tip}). This is shown in fig. 4. The angle between the airfoil chord line and the airflow it interacts with is called the angle of attack (α). This angle shifts if airspeed changes (with a constant ω), and the blade must therefore be rotated to retain optimal performance.

Increasing the angle of attack outside the optimal envelope

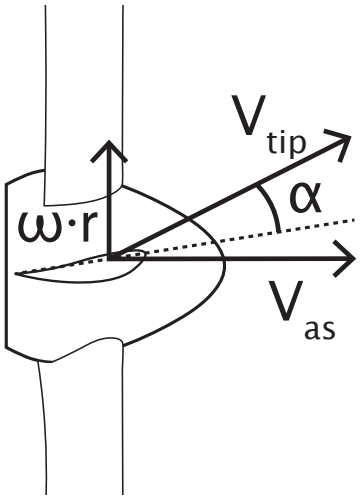

Figure 4: Illustration of propeller relative tip velocity and air speed, resulting the tip velocity.

increases torque and can be utilized during acceleration. If α is decreased sufficiently, the propeller is *feathered*, and no thrust is produced while operating at nominal rpm.

A limiting factor for the propeller rotational speed—and the aircraft cruising speed—is the experienced speed of the propeller tip, where angular velocity is the highest. If the airflow speed across the airfoil approaches supersonic velocities, a reduction in efficiency occurs. This reduction is mainly due to two phenomena. Shock waves start forming, and airflow separates, causing decreased lift and increased drag.

$$M_{tip} = \frac{V_{tip}}{a} \tag{2}$$

The propeller tip speed relative to the speed of sound is called the Mach number (M_{tip}), which can be calculated using eq. (2). This number can be used to define the maximum rotational speed of a propeller. Advanced turboprops are able to operate in sub- to transonic velocities ($M_{tip} \leq 0.8$–1.2).

The physical speed of sound varies with altitude due to air pressure. Keeping rotational speed fixed, a propeller operating at Mach 1 at sea level will have a tip speed of 1.05 if ascending to a cruise altitude of 13 000 ft [6].

$$V_{tip} = \sqrt{(n\frac{2\pi}{60}\frac{D_{prop}}{2})^2 + V_{as}^2} \tag{3}$$

As fixed speed propellers operate at a narrow band of rpms, they also keep a relatively constant Mach tip speed. Tip velocity is proportional to propeller diameter, rotational velocity, as well as aircraft airspeed shown in eq. (3). By using this equation, it is possible to approximate a propeller typical rpm based on a selected tip Mach number, as shown in eq. (4).

$$n_{approx} = \frac{2}{D_{prop}}\frac{60}{2\pi}\sqrt{(aM_{tip})^2 - V_{as}^2} \tag{4}$$

Propulsion efficiency is of significant importance for electric aircraft. When calculating the efficiency of a propeller, a simplified expression known as the ideal propulsive efficiency can be used, shown in eq. (5) [6]. This expression shows that efficiency is higher for a propeller accelerating large quantities of air by a small amount than for one accelerating small amounts of air significantly. In terms of traditional aircraft, this generally means that a large-diameter slowly rotating propeller is more efficient than a small fan rotating quickly.

$$\eta_p \cong \frac{2}{1 + (V_{exhaust}/V_{inlet})} \tag{5}$$

B. Flight Profile

Typical civilian turboprop aircraft are regional or commuter airplanes, meaning they operate across relatively short distances. Studying the electrification of air travel, it is short-haul flights that are most easily electrified [5].

A typical flight can be divided into four stages. Taxiing on the ground both before and after a flight, take off and initial climb, cruising, as well as approach and landing. These phases have different power requirements, which can be simulated on the electrical motors designed in this thesis.

The most power-intensive flight phase is during take-off, where constant maximum power is required during the first minute of flight. After this, power is gradually reduced during climb to around 65% during cruise. This power level is maintained until approach and landing, where motor power is further reduced to 10–25%. There may be a rise in power requirements above these values during the approach as the aircraft needs adjustments to attain the proper glide slope. A typical flight has an average power demand of 53%. During taxi, the power consumption is low enough that studying it further is deemed unnecessary [17]. A diagram of this mission profile can be seen in fig. 5.

As previously mentioned, even though most turboprop aircraft have fixed speed propellers, rpm can typically change based on flight phase. Under normal circumstances, rpm is increased only during take-off, and the relative amount of increase varies from aircraft to aircraft. By examining a few examples, this thesis assumes an RPM change of up to 25% can occur [18, 19].

C. Analytical Motor Dimensioning

The analytical dimensioning workflow described in this subsection is summarized from previous work conducted by the author [15], which is partly developed from the method described Vaschetto et al. [20].

The electric motor dimensioning process starts with calculating initial parameters like rated torque, electrical frequency, and the number of slots per pole per phase. This calculation is done based on input data and applying eqs. (1) and (6).

$$f_{el} = \frac{pN_r}{260} \qquad q = \frac{N_s}{3p} \tag{6}$$

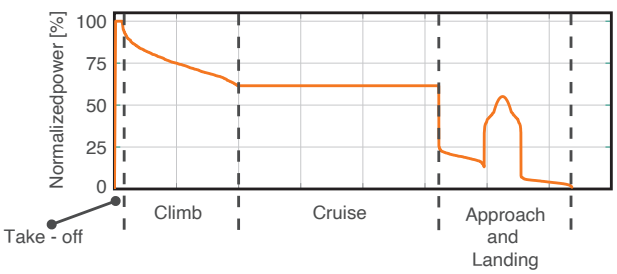

Figure 5: Typical regional flight profile. Adapted from Jux et al. [17]

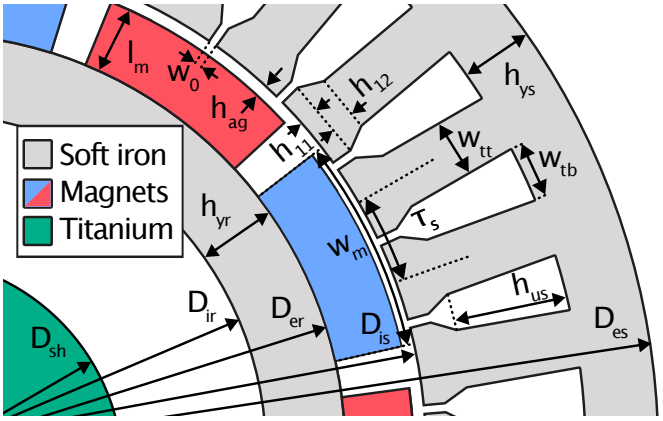

Figure 6: Motor geometric parameters

From here, initial geometric dimensioning of the motor can begin, ensuring that the geometric relationships shown in fig. 6 are fulfilled by requiring eqs. (7) to (9) to be satisfied.

$$D_{ag} = D_{er} + h_{ag} + l_m \qquad L_{\text{cr}} = \lambda D_{ag} \tag{7}$$

$$D_{is} = D_{ag} + h_{ag} \qquad D_{h1} = D_{er} + 2(h_{11} + h_{12}) \tag{8}$$

$$\tau_p = \frac{\pi D_{is}}{p} \qquad \tau_s = \frac{\pi D_{is}}{N_s} \qquad w_m = \alpha_m \tau_r \tag{9}$$

Additionally, other geometric parameters can be calculated as shown in eqs. 10.

$$h'_{ag} = \frac{h_{ag}}{C} \qquad h_{yr} = \frac{D_{er} - D_{ir}}{2} \qquad l'_m = \frac{l_m}{\mu_r} \tag{10}$$

The Carter coefficient, required for calculating equivalent air gap height—which compensates for variations in air gap flux density—is calculated according to eq. (11) [21].

$$C = \frac{\tau_s}{\tau_s - \frac{w_0^2}{w_0 + 5h_{ag}}} \tag{11}$$

After the initial geometric parameters are determined, electromagnetic parameters can be found using eqs. (12) and (13).

$$B_g = B_r \frac{l'_m}{l'_m + h'_{ag}} \tag{12}$$

$$\phi_p = B_g w_m L_{\text{cr}} \qquad B_{yr} = \frac{\frac{\phi_p}{2}}{h_{yr} L_{\text{cr}}\, K_i} \tag{13}$$

Based on these parameters, geometric dimensioning from flux density can take place per eqs. (14) and (15). The latter of these equations is adapted for concentrated winding motors.

$$h_{ys} = \frac{B_g}{B_{\max} K_i} \frac{\alpha_m \tau_p}{2} \tag{14}$$

$$w_{tt} = \frac{B_g}{B_{\max} K_i} \left[\alpha_m \tau_p - \frac{(\tau_s - \tau_p)}{2} \right] \tag{15}$$

Before the remaining geometric parameters can be calculated, the winding factor (k_{wdg}) and the linear current density (K_i) are found using eqs. (16) and (17). The winding factor must be calculated using a method described by Skaar et al. [22] due to the concentrated windings of the motors, where $gcd(a, b)$ is the greatest common divisor for the integers a and b.

$$K_s = \frac{T_r}{\frac{\sqrt{2}\pi}{4} B_{g1} D_{ag}^2 L_{cr}} \tag{16}$$

$$z = \frac{N_s}{gcd(N_s, 3p)} \qquad k_{wnd} = \cos\left(\frac{3\pi q - \pi}{6q}\right) \frac{\sin(\frac{\pi}{6})}{z \sin(\frac{\pi}{6z})} \tag{17}$$

Geometric dimensioning can now be finalized by applying eqs. (18) to (20).

$$A_{us} = \frac{K_s \pi D_{h1}}{2J N_s k_{wdg} k_{fill}} \qquad w_{st} = \frac{\pi D_{h1}}{N_s} - w_{tt} \tag{18}$$

$$w_{sb} = \left[\pi \frac{D_{h1} + 2h_{us}}{N_s}\right] - w_{tb} \qquad w_{sw} = \tau_s - w_0 \tag{19}$$

$$h_{us} = \frac{-w_{st} + \sqrt{w_{st}^2 + \frac{4\pi A_{us}}{N_s}}}{2\pi / N_s} \tag{20}$$

After the geometric sizing algorithm is completed, loss approximations can be made. In this part of the algorithm all parameter equations eqs. (22) and (25) to (27) are prepared and solved while excluding all N_{ph}-terms as in eq. (28). N_{ph} is then calculated according to eq. (29).

First, an approximation of copper area per slot is made in eq. (21).

$$A_{\text{wire}} = A_{us} k_{fill} \frac{N_s}{3 N_{ph}} \tag{21}$$

Per-phase resistance can be approximated using eq. (22), inserting eq. (21) and eq. (30).

$$R_s = \rho \frac{L_{\text{turn}}}{A_{\text{wire}}} \frac{N_{ph}}{2} \tag{22}$$

The resistivity of the copper material is dependent on temperature, and can be extrapolated for a selected operating

temperature T_o by eq. (22). The required coefficients are shown in table I.

$$\rho(T_o) = \rho_0 \left[1 + K_c \left(T_o - 20[^\circ C]\right)\right] \tag{23}$$

The slot leakage inductance (L_s), end winding inductance (L_{end}), and the magnetizing inductance (L_{gap}) are all calculated separately for each slot, as shown in eqs. (24a) to (24c) [24].

$$L_{end} = N_{ph}^2 \frac{\mu_0 \tau_s}{4} \ln\left(\tau_s \sqrt{\frac{\pi}{2A_{us}}}\right) \tag{24a}$$

$$L_{gap} = N_{ph}^2 \frac{\mu_0 \mu_r \tau_s L_{co}}{2\left(l_m + k_c \mu_r h_{ag}\right)} \tag{24b}$$

$$L_s = N_{ph}^2 \left(\frac{\mu_0 h_{us} L}{3 w_{sb}} + \frac{\mu_0 h_{12} L}{\left(w_o + w_{sb}\right)/2} + \frac{\mu_0 h_{11} L}{w_o}\right) \tag{24c}$$

Total motor inductance is now the sum of each contribution multiplied by the slot number, as in eq. (25).

$$X_s = 2\pi f_{el} N_s \left(L_{end} + L_{gap} + L_s\right) \tag{25}$$

Remaining electrical parameters are calculated according to eqs. (26) and (27).

$$E_0 = 4.44 f_{el} k_{wdg} \phi_{p1} \frac{N_{ph}}{2} \tag{26}$$

$$I_r = J_{\max} A_{us} k_{fill} \frac{N_s}{3 N_{ph}} \tag{27}$$

$$\begin{aligned} R_s &= K_1 N_{ph}^2 & X_s &= K_2 N_{ph}^2 \\ E_0 &= K_3 N_{ph} & I_r &= K_4 / N_{ph} \end{aligned} \tag{28}$$

$$N_{ph} = \frac{V_r}{\sqrt{\left(K_3 + K_1 K_4\right)^2 + \left(K_2 K_4\right)^2}} \tag{29}$$

Calculation of the completed motor design mass is purely geometrical, with the exemption of winding mass, which includes approximated end winding mass. This approximation is made by approximating the end winding length as the circumference of a semi-circle between each slot as seen in eq. (30)

$$L_{\text{turn}} = 2\left(L_{ew} + L_{cr}\right) \qquad L_{ew} = \tau_s \frac{\pi}{2} \tag{30}$$

Mass is calculated according to eqs. (31) to (38). A basic motor enclosure weight can be estimated by assuming its mass as a fraction of the total mass in eq. (38).

Table I:
Copper resistivity extrapolation parameters [23]

K_c	ρ_0
$4.290 \cdot 10^{-3}$ $[K^{-1}]$	$1.724 \cdot 10^{-8}$ $[\Omega m]$

$$M_{sh} = \rho_{hs} \pi \left(\frac{D_{sh}}{2}\right)^2 L_{cr}, \tag{31}$$

$$M_{yr} = \rho_{fe} \pi \left[\left(\frac{D_{er}}{2}\right)^2 - \left(\frac{D_{ir}}{2}\right)^2\right] L_{cr}, \tag{32}$$

$$M_{pm} = \rho_{pm} \alpha_m \pi \left[\left(\frac{D_{er}}{2} + l_m\right)^2 - \left(\frac{D_{er}}{2}\right)^2\right] L_{cr}, \tag{33}$$

$$\begin{aligned} M_{tth} = \rho_{fe} N_s \Big[& w_{tt} h_{us} + w_{sw} h_{11} + w_{tt} h_{12} \\ & + \frac{1}{2}\left(w_{sw} - w_{tt}\right) h_{12}\Big] L_{cr}, \end{aligned} \tag{34}$$

$$M_{cu} = \rho_{cu} A_{us} k_{fill} N_s L_{turn}, \tag{35}$$

$$M_{ys} = \rho_{fe} \pi \left[\left(\frac{D_{es}}{2}\right)^2 - \left(\frac{D_{es}}{2} - h_{ys}\right)^2\right] L_{cr}, \tag{36}$$

$$\begin{aligned} M_{enc} = \frac{\xi enc}{1 - \xi enc} \Big(& M_{sh} + M_{yr} \\ & + M_{pm} + M_{tth} + M_{ys}\Big) \end{aligned} \tag{37}$$

$$M_{tot} = \sum_{i=sh,yr,\ \ldots} M_i \tag{38}$$

A basic analytical loss calculation can now be made. Ohmic losses are calculated using eq. (39), while motor iron losses can be approximated using eq. (40) [25]. The Steinmetz coefficients k_s, α_s, and β_s are material specific and can be found by basic curve-fitting.

$$P_{ohmic} = 3 R_s I_r^2 \tag{39}$$

$$p_{iron} = k_s\left((M_{ys} + M_{tth}) B_{ys}^{\beta_s} + M_{rotor} B_{yr}^{\beta_s}\right) f_{el}^{\alpha_s} \tag{40}$$

D. FEM Analysis Loss Calculations

After the initial analytical design process is completed, the next step is to verify these results by numerical means. Numerical simulation of the electrical fields in the motors paints an accurate picture of magnetic dynamics during operation, allowing for more confidence in the discussion and conclusions around a selection of the analytically generated motor designs.

In order to calculate losses, specifically in the motor iron, it is beneficial to separate the losses into multiple components, namely hysteresis losses, eddy current losses, and anomalous losses. This separation is impossible to measure physically but can be a practical design tool when attempting to identify the cause of losses [26]. The sum of P_{hys}, P_{eddy},P_{an} make up an approximation of the motor iron losses, as shown in eq. (41).

$$p_{iron} = p_{hys} + p_{eddy} + p_{an} \tag{41}$$

Grounded in the loss separation described above, one can apply the Bertotti loss model in the frequency domain, as seen in eq. (42) [27]. In this equation, loss density ($p\ [W/kg]$) can be estimated based on peak flux density $\hat{B}$ and flux change frequency (f). In addition, the equation consists of four coefficients K_{hys}, K_{eddy}, K_{an} and α_b, where the three first are tied to each respective component in eq. (41). The coefficient α_b is used to estimate hysteresis losses together with K_{hys}.

$$p_{iron} = K_{hys}\hat{B_{fe}}^{\alpha_b} f + K_{eddy}\hat{B_{fe}}^{2} f^2 + K_{an}\hat{B_{fe}}^{1.5} f^{1.5} \quad (42)$$

The aforementioned constants from eq. (42) are material-specific and can typically be estimated based on material loss data from the supplier, using curve-fitting or other means. Onwards, the Bertotti loss estimation method can be moved from the frequency domain to the time domain by adapting the method described by Fiorillo and Novikov [28]. The equations for these loss estimations can be seen in eqs. (43) to (45). As an added benefit, this method allows for the used flux waveforms to be non-sinusoidal, in contrast to eq. (42) in the frequency domain which is only valid for the first harmonic.

Hysteresis losses occur in any ferromagnetic material subjected to an alternating magnetic field. Domains of material atoms are aligned in different magnetic orientations, and subjecting this material to an electric field causes these atom groups to align to the external field. While the domains in the ferromagnetic material gradually align, each orientation change—called a Barkhausen jump—causes energy losses in the form of heating.

The stator iron is especially subject to a rapidly altering magnetic field. The material is subjected to two opposite peak flux densities for every half cycle, and losses increase by increased electrical frequency and peak flux. This behavior is reflected in the hysteresis loss estimation equation shown in eq. (43), which includes peak flux density ($\hat{B}$), electrical period (T_{el}), as well as two material-specific constants K_h and α_b.

$$p_{hys} = \frac{K_h \hat{B}^{\alpha_b}}{T_{el}} \quad (43)$$

Eddy current losses are caused by ohmic losses from magnetically induced looping currents in the motor iron, as well as in the motor magnets. As per Faraday's law of induction, the currents increase in magnitude with increased flux change, magnetic field strength, and the size of the current loops. In order to reduce iron losses, motor iron is divided axially into sheets that negate the possibility of large current loops. An illustration of this principle can be seen in fig. 7 The ohmic iron losses themselves can be reduced by having iron materials with lower conductivity, increasing their internal resistance.

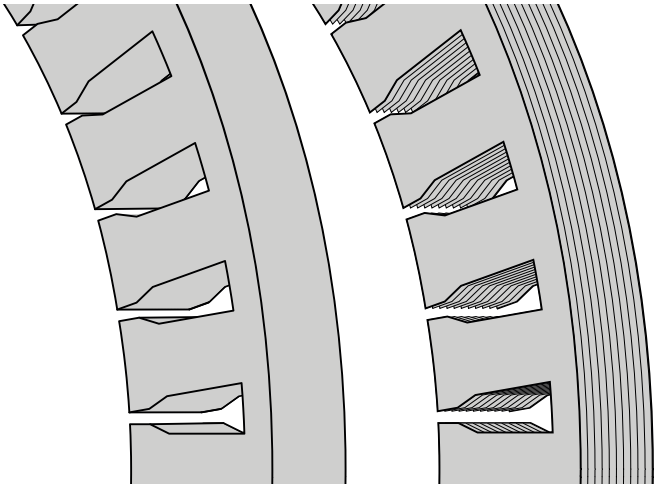

Figure 7: Un-sheeted (left) and sheeted stator (right).

$$p_{eddy} = \frac{K_{eddy}}{2\pi^2 T} \int_0^T \left|\frac{dB}{dT}\right|^2 dt \quad (44)$$

Lastly, there are *anomalous losses*. These are iron losses, caused by remaining factors like physical distortion in the iron material. These losses can be approximated by eq. (45).

$$p_{an} = \frac{K_a}{8.76T} \int_0^T \left|\frac{dB}{dT}\right|^{1.5} dt \quad (45)$$

III. Aircraft data sampling

Current fossil-driven aviation uses one of several types of motors. This thesis searches to examine the design of electric motors designed based on the performance of these fossil motors. In order to constrict the scope of the analysis, it is necessary to reduce this selection of motor types to a single type: turboprop motors.

As the thesis studies electric motor design for use in traditional aircraft, focusing on efficiency is paramount. Since turboprops are more effective than turbofan regional aircraft [7], these aircraft may form a better foundation for efficient propulsion design. Part of the reason for this is that turbojets operate at much higher air speeds and therefore have a larger velocity gradient between V_{inlet} and $V_{exhaust}$, leading to lower efficiency per. eq. (5).

In order to form a foundation for the design of electric motors, a broad selection of turboprop-aircraft data is sampled. The data within this section was initially sampled in the previously mentioned pre-thesis report [15]. The complete dataset is presented in table II.

Sampled data consist almost exclusively of twin-engined aircraft and includes most of the regional turboprop aircraft used in civilian flights. Passenger capacities range from 9–90 persons, and both certification classes by the European Union Aviation Safety Agency (EASA)—CS-23 and CS-

Table II: Aircraft data.
*Approximated data.

Manufacturer	Model	Max. pax. cap.	D_{prop}	N_{motors}	Single engine power [kW]	Motor	V_{max} [m/s]	RPM*	Source
Antonov	AN-140	52	3.6	2	1838	PW127A	159.7	1086	[29]
Antonov	An-32	50	4.7	2	3812	Ivchenko A1-20DM	147.2	869	[30]
Antonov AN-2	AN-2	12	3.6	1	1375	TVD-20	70.8	1325	[31]
ATR	ATR-42-300	50	3.96	2	1342	PWC PW120	138.9	1058	[30]
ATR	ATR-72	74	3.93	2	1846	PW127M	141.7	1058	[30][32]
British Aerospace	Jetsteram Super 31	19	2.69	2	760	Garrett TPE331-12UAR	135.3	1574	[30]
British Aerospace	Jetstream 41	29	2.9	2	1118	Garrett TPE331-14	151.7	1388	[30]
British Aerospace	ATP	72	4.19	2	1978	PW126A	140.4	996	[30]
CASA/IPTN	CN235-100	44	3.35	2	1305	GE CT7-C	126.1	1294	[30]
de Havilland Canada	Dash-8-100A	39	3.96	2	1524	PW121	139.2	1057	[33]
de Havilland Canada	Dash-8-Q200	40	3.96	2	1600	PW123D	148.6	1027	[34]
de Havilland Canada	Dash-8-Q300	56	3.96	2	1864	PW123B	147.8	1030	[30][35]
de Havilland Canada	Dash-8-Q400	90	4.1	2	3781	PW150	185.3	847	[36]
Dornier	328	33	3.6	2	1625	PW119C	172.2	1031	[37]
Embraer	Brasilia EMB-120	30	3.2	2	1342	PW118	168.9	1177	[30]
Fairchild	Metro 23	20	2.69	2	820	Garret TPE331	160.0	1452	[30]
Fokker	50-100	58	3.66	2	1864	PW125B	156.9	1079	[30]
Fokker	F27	59	3.66	2	1529	RR D Mk.539-7R	141.4	1137	[38, 39]
Ilyushin	Il-114	64	3.6	2	1839	Klimov TV7-117S	138.9	1164	[40]
LET	L-410 UVP-E20	19	2.4	2	597	GE H80-200	112.5	1862	[41]
Piper	PA-42-III	9	2.7	2	537	Garrett TPE331-14	126.0	1606	[42]
Shorts	330-200	30	2.82	2	893	PW PT6a-45-R	97.2	1631	[30]
Shorts	360	36	2.82	2	1062	PW PT6A-65AR	112.2	1586	[43]
Sukhoi	SU-80	30	3.96	2	1305	GE CT7-9B	130.6	1083	[44]
SAAB	340B	37	3.35	2	1305	GE CT7-9B	141.1	1243	[30]
SAAB	2000	58	3.81	2	3096	RR AE2100P	184.7	915	[30]
Xian	MA60	62	3.93	2	2750	PW127J	142.8	1054	[40]

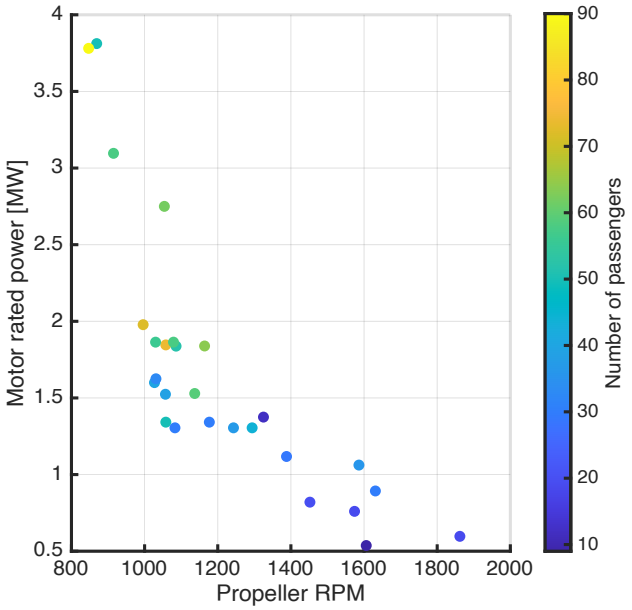

Figure 8: Sampled civilian turboprop aircraft.

25—are represented. Both small commuter aircraft and the largest turboprop airliners are thus included.

Aircraft engine rated power data is readily available; however, information about the rated rotational speed for their propellers is not as trivial to source. This lack of information is partly caused by existing turbo-motors rarely being direct-drive, and that rated motor-rpm, therefore, is different according to which aircraft/propeller is operated by it. Rated RPM for direct drive propulsion must therefore be approximated. The propeller tip speed is assumed to be fixed at Mach 0.8 for all aircraft. Using eq. (4), propeller diameter and aircraft maximum air-speed, n_r can be approximated. The sound speed value is based on the *U.S. standard atmosphere* at 13 000 ft (4000m)—where $a = 324.579$ m/s—for all aircraft [45].

These data can be used to plot the aircraft performances across the design space previously described, as presented in fig. 8. In order to form a picture if the capabilities of the sampled aircraft, passenger capacity is also included in the diagram.

In fig. 8, the motor output power is considered together with propeller rpm and not turbine rpm. Although turbine power and rpm form an accurate description of turbine motor performance, the scope of this thesis is to examine the propeller-motor interface—particularly with an electric motor directly driving a propeller. Therefore, considering propeller rpm and shaft power is more relevant in the context of this thesis.

IV. Electric Motor Design

This section will describe the electric motor design processes conducted during this thesis. The foundation for most of these choices is also described.

The goals of the design process can be divided into two aspects. Firstly initial design space parameters of motor power rating and rotational speed must be realized. Secondly, choices must be made during the process to realize a specific objective, reflecting desired performance. It is decided that motor efficiency and specific power are the most important variables to optimize for.

In its essence, the design process of an electric motor consists of two steps.

First, a decision on motor type must be made. Initially, this spans topology, where the option of axial to radial flux, salient to non-salient poles, geared or direct drive, cooling method, and motor type must be decided. Beyond—parameters like pole count and aspect ratio can be chosen. After selecting a base topology, one must select a basic winding design. This encompasses slot count and winding topology. After this, motor materials can be chosen based on desired performance goals. Lastly, and before the second design process step, some initial geometric parameters are assigned values.

Second, the actual motor design must be found, which includes finding actual geometric dimensions and stating electrical parameters. These calculations are, in turn, performed employing an analytical design algorithm. After this, the resulting designs can be verified by more advanced simulations of the motor performance and the geometric parameters tweaked to improve overall motor performance.

The choices in design determined in this section are based on a literature review conducted during this the pre-project for this thesis [15].

A. Underlying Motor Topology and Parameters

The initial choice of topology and design parameters must be made to complement the design requirements of electric motors for aviation. These requirements can be considered as two main elements. The demands of an electric motor in aviation and the performance demanded by the sampled aircraft.

For civilian electric aviation in general, two of the most essential aspects are efficiency and specific power, which are the two design outputs addressed in this thesis. This prioritization means making choices that allow for high efficiency and lightweight construction.

Building geometry that balances efficiency and weight is challenging, as these two factors often come at a cost to each other. Increasing efficiency reduces battery capacity demands, saving weight but ofttimes making motors heavier. The examination of energy storage is considered outside of the scope of this thesis. This scope restraint means that the work will attempt to avoid direct choices of trading efficiency for specific power.

The aircraft data from section III show that turboprop motor outputs power in the range of 0.5–4 MW while driving propellers in the speed range of 800–2000 rpm. The decreasing rpm as a function of increased power output means that the aircraft demand relatively high torque, which must be accounted for in the motor design. This torque demand is further amplified by the generally low rpm of aeronautical electric motors compared to automotive motors.

1) Base Topology Selection: The permanent magnet synchronous machine (PMSM) is a popular type among the many kinds of electric motors. The use of permanent magnets mean that the rotor core is permanently magnetized, negating losses related to electrical magnetization. The technology is mature, and the topology has already seen use in aviation due to its high power density and efficiency [4, 46, 47]. It is therefore elected to design PMSMs in this thesis.

Multiple types of PMSMs exist, with the radial flux inner rotor PMSM being the most common. *Radial flux* machines mean the magnetic coupling between stator and rotor takes place radially from the motor core, with the rotor either being inside or outside the stator. The alternative—*axial flux* machines—are characterized by the stator and rotor being placed along the motor shaft and the magnetic coupling being situated axially along the shaft. Even though axial flux machines show promise in their compactness and specific power, they are less technologically mature than radial flux machines. Consequently, the PM machines in this thesis are all radial flux machines.

A radial flux PMSM can either have its rotor inside the stator, outside it, or two rotors on either side of the stator. NASA's SCEPTOR program evaluated these three designs and concluded that the double rotor design achieves higher efficiency and specific power than both in-, and out-runner motors [47]. However, the increased complexity led to the more traditional in-runner motor being selected as the base topology in the project.

For the reasons outlined in this subsection, the radial flux, inner rotor, PMSM is selected as the base topology for all motors designed in this thesis.

It is determined to use liquid cooling in the motor, as this method can handle a higher slot current density than air-cooled machines without overheating. A higher allowable current density means that a smaller slot area is needed, reducing weight [48].

2) Initial Magnetic Design: Selection of the pole count is made outside the dimensioning algorithm and is therefore not an optimization variable. Because of this, the choice must be made based on literature to achieve satisfactory

results across the design space. According to Zhang et al. [13], high specific power motors generally employ "high pole counts"—a claim that is backed up in other literature [49, 50]. Dubois et al. [47] also find that pole counts between 48 or 50 poles achieve higher efficiency at a lower weight than lower count motors. It is elected to utilize a pole count of 40 in the motor design.

The two main options in permanent magnet mounting are surface mounted PMs (SPM) or interior mounted magnets (IPM), where magnets are shrouded inside the rotor structure.

There are two main benefits of interior mounted magnets. The first is that they do not require structural support in the rotor to combat the radial forces experienced during rotational velocity, making it possible to reduce air gap height [51]. The reduced air gap leads to less leakage flux. The other benefit—in many cases—is that they offer a high torque across a wide speed range, contrary to SPMs that typically have a higher torque output across a narrower band of rotational velocity [13].

Surface-mounted magnets often require a retaining ring to secure the magnets to the rotor surface, increasing the air gap. However, based on aircraft data not requiring high rotational velocities, it is assumed that the radial load on the magnets is low enough to allow for a sufficiently small air gap. The relatively narrow torque-speed characteristic of the SPM may be a benefit considering the design requirements posed by fixed the speed propellers of turboprop aircraft. Because of this, an SPM-design is pursued further.

3) Winding Topology: Laying the foundation for the electric dimensioning of the motor, the choice of winding topology must be made.

The two main winding architectures are concentrated and distributed windings. In distributed windings, where $q \geq 1$ from eq. (6), ends of the windings span across multiple slots and overlap around the stator periphery. This layout generally reduces induced EMF harmonics [52, 53]. Concentrated windings, however, where $q \leq 1$, is characterized by end windings only traversing single teeth. This shorter traverse reduces end winding length, which leads to lower total mass and reduced end winding ohmic losses. Concentrated winding offers desirable benefits and is selected as winding architecture for the project.

The slot number selection is made based on the choice of concentrated windings. In order to achieve a high winding factor, eq. (17) shows that some combinations of pole count and slot count are more desirable than others. A slot count of $N_p = 45$ is selected based on two main factors. The winding factor of this slot count is 0.9452, which is satisfactorily high. Additionally, the greatest common divisor of slot count and pole count is 5, allowing for faster computations as only 1/5 of the motor needs to be simulated.

A slot count of 45 means that the three-phase windings must be double-slotted. The winding layout for all designs in this thesis is shown in fig. 9.

A voltage rating must be set for the motor designs during the electrical dimensioning process. A V_r of 1 kV is used as a base parameter for all motors. Electrical dimensioning during the FEM-analysis is further described in section IV-C2.

4) Materials selection: Materials must be selected for motor iron, permanent magnets, coils, and the motor shaft. These decisions are made to promote the desired performance parameters, namely density, and ability to handle magnetic and physical loading.

Due to the high torque the motors experience during full-power operation, a high motor iron flux density is required to reduce the need for motor iron. This requirement can be deduced from eq. (16). The material magnetic permeability describes the ability of the material to conduct magnetic flux before reaching a maximum and the iron becoming saturated. Having a high permeability and a low density is, therefore, the ideal iron material based on the considerations in this project.

Two alloys are considered for motor iron, namely cobalt-iron (CoFe) and silicon-iron (SiFe), with saturation flux and mass density for both shown in table III. Both materials are known for their high saturation flux, but ultimately CoFe alloys have the highest [4, 54, 55]. SiFe-irons are cheaper and more widely used, but based on their higher saturation flux, the CoFe alloy Vacoflox 48 [56] is selected as motor iron material.

Motor magnets are selected based on remanence flux density (B_r) and magnetic coercivity (H_c). Remanence flux density describes the amount of magnetization in the magnet material, where table IV shows these values for the three considered magnet materials. In order to conserve mass, a high remanence is desirable, where NdFeB-magnets are the superior choice. NdFeB is also the material with the highest coercivity. One downside with NdFeB-magnets are their low curie-temperature as compared to SmCo and AlNiCo-magnets [58, 59]. This means that they can be demagnetized at lower temperatures than their counterparts. However, since the Curie temperature of NdFeB is 300–370

Table III:
Soft magnetic steel [54, 55, 56, 57].

Material	B_{sat} **[T]**	ρ **[kg /m^3]**
CoFe	2.3	8120
SiFe	2.05	7600 –7800

Table IV:
Permanent magnet materials [58, 59]

Material	B_r**[T]**	H_c**[kAm^{-1}]**
NdFeB	0.97 – 1.45	740 – 1000
SmCo	0.85 – 1.1	620 – 840
AlNiCo	0.6 – 1.16	40 – 120

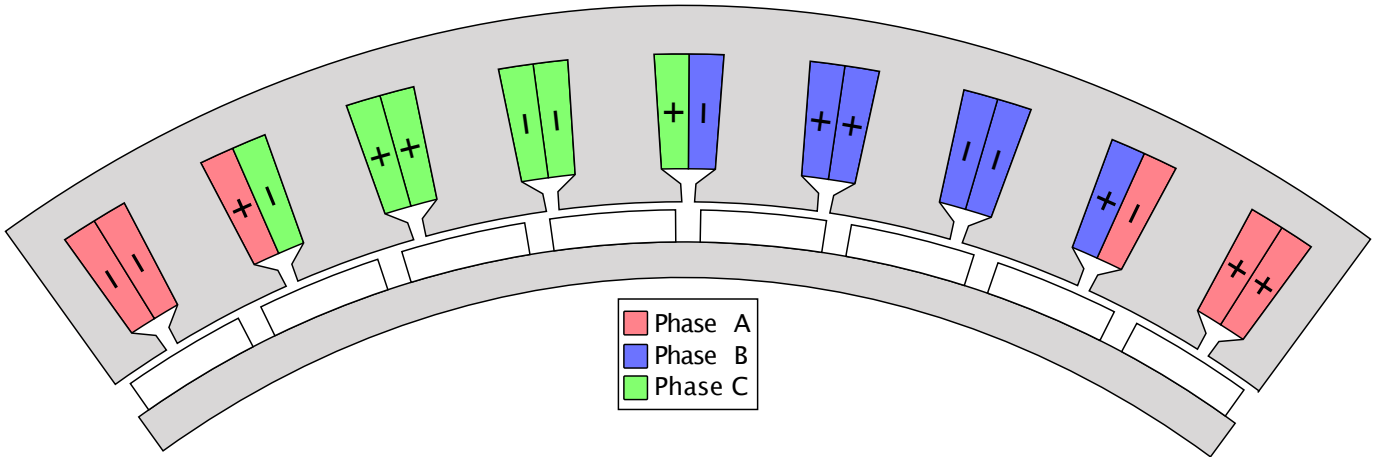

Figure 9: Winding layout for 40-pole–45-slot PMSM with concentrated windings.

°C, it is considered sufficiently high, and this material is therefore selected. The specific magnet grade selected is N52M.

Material parameters are also required for coils and the motor shaft. Copper is selected as the winding material. Due to its tensile strength and low density, grade 5 titanium is selected as shaft material.

5) Geometric design parameters: The analytical design algorithm described in section IV-B requires an initial parameter of motor aspect ratio—λ. This value describes the ratio between motor length and the air gap diameter. A high λ means the motor is more barrel-shaped, reducing inner motor radius and volumetric size. Qu et al. [50] shows that designing a motor with a low aspect ratio can result in efficiency gains as well as higher specific power. As these parameters are the main optimization focus in this thesis, a low aspect ratio of $\lambda = 0.2$ is selected.

Due to uncertainty about radial forces, and the choice of keeping structural analysis outside the scope of the thesis, the retaining sleeve in the air gap made to keep the permanent magnets in place is not modeled. However, the air gap height is set to 2.5 mm to ensure the room for such a sleeve.

In addition to λ, slot fill factor, air gap size, shoe dimensions, operating temperature, and magnet to pole pitch is determined—which will remain constant for all designs. The parameters are presented in table VI.

Table V:
Material specific analytical input properties.

Symbol	Value	Source
B_{max}	1.850 T	[56]
k_i	0.970	[60]
B_r	1.445 T	[61]
$\alpha_s/\beta_s/k_s$	1.879 / 2891 / $1.04 \cdot 10^{-4}$	[56]
J_{max}	4.950 A/mm^2	[62, p.313]
ρ_{iron}	8120 kg/m^3	[56]
ρ_{mag}	7500 kg/m^3	[61]
ρ_{cu}	8933 kg/m^3	[23]
ρ_{sh}	4430 kg/m^3	[63]

Shaft diameter is based on the material properties of titanium and the expected maximum torque for the machines. The diameter of 100 mm is deemed sufficient for all motor ratings [64, 63]. Magnet pitch as a fraction of pole pitch is set to 5/6, where a larger value can cause excessive flux leakage Strous [65].

Any structural analysis will not be conducted during the design process—to limit the scope of the thesis. An approximation of the enclosure mass will be made instead based on a PMSM designed for the 2010 hybrid-electric vehicle Toyota Prius. This design has a total enclosure mass of 38.3% of the total unit weight [66]. Since this motor design is made for vehicular propulsion, it is assumed that the focus is less on minimizing weight than on aeronautical motors. Enclosure mass is therefore assumed to be 25% of the total machine weight.

B. Analytical Design Algorithm

An analytical design algorithm is made in order to generate the electric motor design space. The analytical equations described in section II-C form the basis for the methodology laid out in fig. 10.

The generation of a design space across different motor performance parameters is initialized by selecting which parameters the design will span. As previously specified, the electric motors designed in this thesis will be compared to the rated power of turboprop aircraft. After aircraft rpm data is made available, it is possible to use motor speed and power rating as the main input parameters for the design space. The parameters for this sweep are presented in table VII.

At each power and speed requirement, a series of steps are conducted. A motor is designed based on the initial dimensioning equations from section II-C, with the rotor

Table VI:
Input parameters for all analytical dimensioning.

V_r	p	N_s	k_{fill}	α_m	l_m	h_{ag}	h_{11}	h_{12}	D_{sh}	w_o	T_o
1000 V	40	45	0.45	5/6	10 mm	2.5 mm	2 mm	2 mm	100 mm	4 mm	60 °C

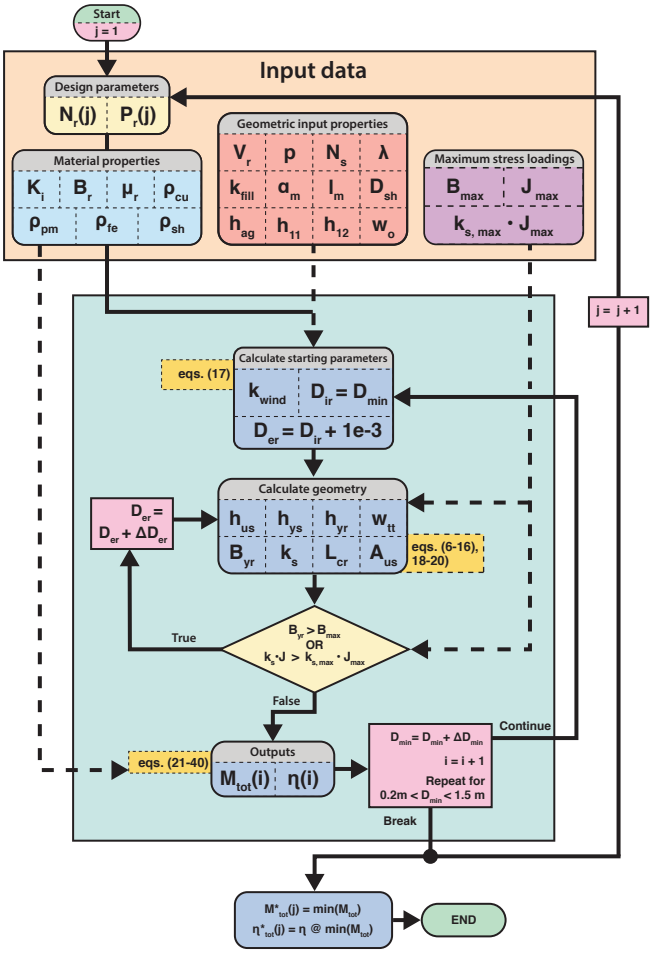

Figure 10: Analytical design method flowchart.

Table VII:
Design space parameters.

P_r	N_r	ΔD_{er}	ΔD_{min}
0.5–4 MW	800–2000 rpm	1 mm	5 mm

yoke diameter h_{us} increasing until thermal loading and flux density are lower than the pre-specified limit. This process is conducted for values of D_{min} ranging from 0.2 m to 1.5 m, with a step size of 5 mm. After this, the motor design with the lowest mass is stored, and the process is repeated for new power and speed requirement.

In order to achieve viable designs, constraints are used to manage selected parameters. Flux density in the motor iron is constrained by setting a maximum value based on the characteristics of the selected motor iron material. This value is selected based on the *knee point* of the B–H-characteristic curve of *Vacoflux 48*. The selected value is 1.85 T, representing a relatively high-efficiency operation, after which the motor iron approaches saturation. A thermal loading constraint is also used during initial motor dimensioning. This constraint is expressed as the product of linear current density (K_s) and slot current density (J). According to Bertotti [27], air-cooled machines typically operate with a K_sJ of 1–2 GA^2/m^3, while liquid-cooled machines can reach 3–4 GA^2/m^3. As the motors are selected to be liquid-cooled, the K_sJ-constraint is set to 4 GA^2/m^3.

1) Assumptions and Simplifications: A major simplification in the analytical algorithm lies in the completed efficiency calculations. Using Steinmetz's loss equation, motor iron losses are included, with ohmic losses calculated on a per-phase equivalent basis. B-fields are not modeled, which can cause inaccuracies. In addition, both magnet eddy current losses and AC losses are omitted.

No thermal analysis is conducted, which means that parameters determined by temperature are fixed at an assumed T_o.

No structural simulations or calculations are conducted, as only the active components of the motor are dimensioned. An approximation of enclosure mass is, however, made.

The values in table VI are all kept constant during the analytical dimensioning procedure. There is a possibility that changing these parameters will lead to a performance improvement. However, their inclusion is elected to keep outside the scope of the thesis.

C. FEM — Simulation and Adaptation

After generating an analytically calculated design space of motor designs—and before conducting any analysis of the results—a finite element method (FEM) analysis is to be completed using the software COMSOL Multiphysics [67]. A numerical simulation of a selection of motor designs

generates performance and loss data that can be compared to the values generated by the less sophisticated analytical design algorithm. These results can additionally serve as a base for further design improvement.

1) Geometry Generation: The motor dimension parameters generated by the algorithm described in section IV-B is used to build a 2-dimensional geometry in COMSOL. The geometry is further parameterized in order to reduce the number of required variables in any potential future optimization algorithm, reducing the number of governing geometric parameters to those presented in table VIII.

In order to reduce simulation time, only the most minor fraction possible of the motor should be simulated. The results impacted by this simplification are then compensated for in post-processing. Due to symmetry, this fraction is the inverse of the greatest common divisor between pole count and slot count. As the pole and slot count is fixed during the entire design process, only *one-fifth* of any motor is simulated.

To improve simulation accuracy, the COMSOL mesh builder is set to *fine*. In addition to this, the air gap mesh is further improved to ensure result validity. The number of mesh nodes in the air gap is selected to find a balance between reduced simulation time and result accuracy. The number of elements per pole is set to 70, meaning the air gap in total consists of 560 nodes for 1/5 of the entire motor.

2) Simulation and Loss Modeling: When each motor is simulated in COMSOL, the physics model is in different ways adapted to produce desired results. Multiple sources of losses must be modeled to generate satisfyingly accurate loss approximations of the motor. Motor torque, power output, as well as stator and rotor flux density are also variables to be measured. Some approximations and simplifications in the employed COMSOL physics model are also made.

In order to simulate stator iron flux and eddy-currents, some adaptations to the base materials used in COMSOL are made. The base eddy current model does not take stator iron sheeting into account. Therefore, this model is discarded by omitting motor iron conductivity entirely and using a different loss model to simulate eddy-current losses.

Bertotti's expanded loss model, described in section II-D, using eqs. (43) to (45) is implemented in COMSOL, by adding up losses over the stator iron. To accomplish this, material parameters α_b, K_{hys}, K_{eddy} and K_{an} must be determined. Equation (42) is used as a custom equation the curve fitting tool in Matlab. Based on Krings [68] it is decided to constrain α_b between 1.4 and 2.2—a typical range for this variable. Additionally, all coefficients should be positive, leading to them being constrained accordingly.

Data for the iron material previously described, Vacoflux 48, is provided from the data sheet presented in Vac [56] and used to approximate loss coefficients. The values of these parameters are presented in table IX, while the goodness of the curve fit is presented in table X. The anomalous loss coefficient is bound at the non-negative constraint, meaning anomalous losses are omitted for these simulations. Because of data availability, it is decided to assume a sheet thickness of 3 mm for the motor iron.

The implementation of the previously described Bertotti iron-loss calculations in COMSOL is done by calculating losses according to eqs. (43) and (44) for motor iron every element in the FEM-analysis. Every contribution is then calculated according to the iron surface integrals in eqs. (46) and (47). The final output loss value is the calculated average loss for a single simulation.

$$P_{eddy} = N_{seg} L_{co} \rho_{fe} \iint_S p_{eddy} \mathrm{ds} \tag{46}$$

$$P_{hys} = N_{seg} L_{co} \rho_{fe} \iint_S p_{hys} \mathrm{ds} \tag{47}$$

Calculation of copper losses in COMSOL is done in much the same way as the analytical calculations. Copper temperature is set to the same values as for the analytical calculations to ensure the same conductivity. Resistance is then calculated using eq. (48). Average turn length is calculated according to eq. (30), and therefore includes end winding ohmic losses, even though end windings are not electrically or magnetically modeled.

$$R = \rho \cdot n_{\text{turn}} \cdot \frac{L_{turn}}{A_{slot} \cdot \frac{k_{ftll}}{n_{\text{turn}}}} \cdot \left(\frac{2}{3} \cdot \frac{N_s}{N_{seg}} \right) \tag{48}$$

Magnet eddy current losses are calculated as average losses based on the integrated loss calculation in COMSOL. This result is then multiplied by the total number of motor sections.

In order to calculate motor output torque, Arkkio's method is implemented into the COMSOL model [69]. Due to the motors discussed in this paper being three-phase motors, the largest harmonic component of the torque ripple has a frequency of 6 times the electrical frequency. This frequency means that the average torque, used as an output variable, can be calculated as the time average during a sixth of the electrical period. In order to reduce total simulation time, it is also decided to constrain simulation length to a sixth of the electrical period. Average power-output can be calculated from average torque as per eq. (1).

Maximum flux density measurements are conducted by creating line averages in the rotor and stator yoke as well as in the stator teeth, indicated in fig. 11. During every time step in the total simulation time of $\frac{1}{6}T_{el}$ an average value is calculated. These measurement placements are selected to ensure that a periodic flux density maximum is reached during the reduced simulation time. The rotor yoke measurement—specifically—is placed between two

Table VIII:
Required input parameters for building COMSOL geometry.

α_m	D_{ir}	h_{11}	h_{12}	h_{ag}	h_{us}	h_{yr}	h_{ys}	k_{fill}	l_m	w_{tt}	w_0	λ

Table IX:
Bertotti loss parameters from curve fit.

Name	Value	Unit
α_b	2.2	—
K_{hys}	$8.781 \cdot 10^{-3}$	$[\frac{W}{kg}]$
K_{eddy}	$6.903 \cdot 10^{-5}$	$[\frac{m^2 s^3 A^2}{kg^2}]$
K_{an}	0	—

Table X:
Goodness of curve fit for Bertotti loss estimation.

R-square	**SSE**
98.35%	1368 $\frac{W}{kg}$

opposite magnets, where the flux density is highest. This measurement must also rotate concurrently with the rotor. Flux maxima are then extracted by simply finding the maximum value of each of the three line averages.

Initial attempts to simulate motors based on the electrical parameters calculated using the analytical algorithm described section IV-B yields output power that does not precisely match the desired rating. It is elected to—instead of defining coil-currents—define a current density for each slot and then calculate the coil current by employing eq. (49). Using current density as an input variable makes the management of slot thermal loading more controllable, as it becomes possible to control current density directly. The number of turns is fixed at eight turns per coil for all designs to simplify the electric dimensioning further.

$$\hat{I} = \frac{\sqrt{2} J k_{\text{fill}} \cdot A_{\text{slot}}}{N_{\text{turns}}} \tag{49}$$

Some of the analytically generated electrical parameters do not correspond to the desired power output; sweep analyses of the slot current density are therefore conducted. Through interpolation of the power output of these simulation data, a current density corresponding to the desired output power can be found. A simulation employing this current density is then conducted to ensure the validity of the interpolation, and J is adjusted if necessary.

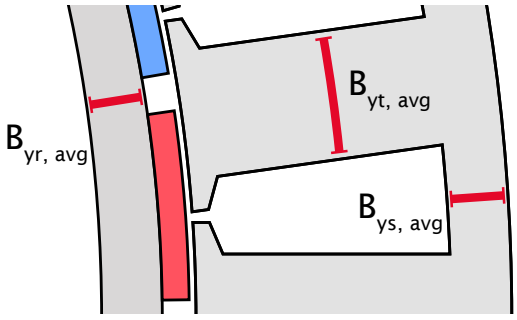

Figure 11: Line averages used to measure different flux densities

Coil currents are in COMSOL described as in eq. (50). An offset angle θ_o is included in the equations to ensure a shift in the electric and mechanical angle that results in maximum torque. The angle is determined by simulating the motor at the rated mechanical speed with no current and identifying the relative phase shift in the induced coil voltage. The angle is 1.512 radians and is assigned to θ_o.

$$\begin{aligned} I_a &= \hat{I} \sin\left(2\pi f_{el} t + \theta_o\right) \\ I_b &= \hat{I} \sin\left(2\pi f_{el} t - 2\pi/3 + \theta_o\right) \\ I_c &= \hat{I} \sin\left(2\pi f_{el} t + 2\pi/3 + \theta_o\right) \end{aligned} \tag{50}$$

3) Comsol Assumptions and simplifications: To reduce the complexity of electrically sizing each motor, the number of coil turns is kept constant during simulations of motors in different sizes. This means that voltage increases by power input while current density is kept in the same range.

The losses simulated in the motor iron are hysteresis, eddy current and anomalous losses. For the magnets, constant magnetization is assumed, and only eddy currents in the magnets are assumed to cause losses. Electrically—only ohmic losses are included. The sampling of loss calculations means that any mechanical and AC losses are not assumed nor approximated.

No thermal analysis will be conducted. Motor performance is calculated assuming an ambient temperature of 60°C, but a thermal circuit is not constructed. Thermal management is instead managed by being included as constraints both during the later manual optimization and the analytical dimension algorithm.

D. Manual Optimization

After completing FEM simulations of a selection of analytically designed motors, it is desirable to investigate the possibility of optimizing and improving the designs further. Conducting this optimization, in turn, makes it possible to validate the analytical design ability of the algorithm to produce efficient and power-dense designs.

The manual optimization procedure will be conducted with the three motor designs implemented in COMSOL as a starting point. The manual optimization of these designs is conducted while keeping the individual initial parameters constant, like power output (P_r) and rated speed (N_r).

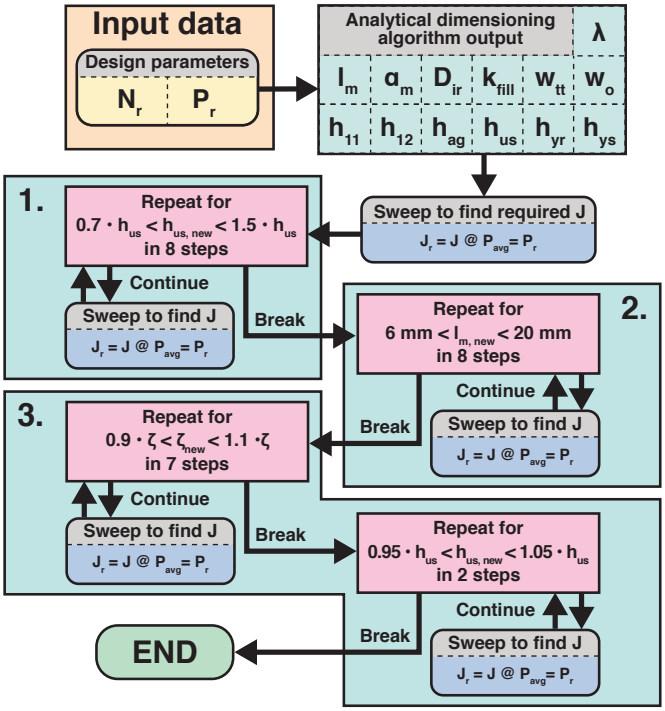

Figure 12: Manual optimization sweep flowchart. In this diagram, ζ represents all iron dimensions h_{yr}, h_{ys} and w_{tt}.

The first part of the manual optimization procedure is to examine the effect of varying tooth length (h_{us}). Constant power output is desired, which means that current density must change with tooth length. A sweep analysis changing the stator tooth length between $0.7 \cdot h_{us}$ and $1.5 \cdot h_{us}$ while applying current densities in the range 3 to 10 A/mm^2 is conducted in COMSOL. More detailed sweep parameters are shown in table XI.

The sweep analysis of stator tooth length generates multiple operating points with different power outputs for each specific tooth length. By using linear interpolation, approximated simulation output data is generated for each tooth at the intended motor power output. These data provide enough information to determine the desired tooth length for each motor performance point. Tooth length has, per eq. (20), a significant impact on slot area and thus slot current density. Investigating this parameter allows optimizing the motor dimensions to a maximum allowable current density based on thermal loading.

The second part of the manual optimization procedure is investigating the performance impact of changing magnet length (l_m).Similarly, as for h_{us}, magnet length is varied with changing current densities. Magnet length has a lower impact on slot area than tooth length, so the range of current densities is smaller than during the previous sweep—reducing simulation time.The sweep variables can be observed in table XII.

The rationale for investigating changes to l_m is that it changes the balance between flux produced by permanent magnets and stator windings, where efficiency or power density may be impacted.

The third and last aspect of the motors to be optimized is iron dimensions, with the intent to improve maximum flux density distribution. Flux density is in terms of iron dimensions mostly affected by rotor yoke height (h_{yr}), stator yoke height (h_{ys}) and tooth width (w_{tt}), which can be seen in eqs. (14) and (15). Sweep parameters are shown in table XIII.

The main goal in optimizing yoke geometry is to reduce the difference in flux density in teeth and stator back iron. A significant difference in stator yoke and stator tooth flux density is undesirable, as one of the two will be loaded harder or less than necessary. If flux density is too high, iron can also be re-dimensioned to improve efficiency.

After the results for the third round of optimization are generated, the rated current density may change based on what changes are elected to be made. Stator tooth height, h_{us}, therefore undergoes one last sweep to keep the final motor design at the desired current density and thermal loading.

E. Performance map

The completed motor design optimization produces final motor designs for retrofit in turboprop aircraft. Base performance results are calculated during the optimization process for motor operation at rated rpm and power output. However, it remains to be seen how the motors perform efficiency-wise during an actual flight profile.

From fig. 5 in section II-B it can be seen that power output changes based on if the aircraft is in take-off, climb, cruise, or an approach/landing phase. Therefore, the finalized designs are subjected to different values of input current to simulate this range of output power. The change in rpm

Table XI:
First sweep analysis parameters

Parameter	*Value range*	*Number of steps*
h_{us}	70–150%	8
J	3–10 A/mm^2	8

Table XII:
Second sweep analysis parameters

Parameter	*Value range*	*Number of steps*
l_m	6–20 mm	8
J	5-9 A/mm^2	5

Table XIII:
Third sweep analysis parameters

Parameter	*Value range*	*Number of steps*
h_{yr}, h_{ys}, w_{tt}	90–100%	7
J	6.4-6.5 A/mm^2	2

fixed speed propellers experience during take-off is also included in the analysis. The specifics of this sweep are shown in table XIV.

Motor power output changes both based on input current and rpm. In order do display efficiency as both power and rpm, interpolation must be conducted. This is achieved through the *griddata*-function in Matlab, making sure that power is correctly attributed to the y-axis of the generated diagrams. The function interpolates the calculated efficiency data across 200 x 200 points.

The power-use sweep results make it possible to superimpose the different flight phases in the final result. The knowledge that motors typically reach their higher rotational speeds during take-off can be used to further generate approximated operating points in the two-dimensional power-rpm diagram.

V. Results

A. Analytical data

The analytical design algorithm described in section IV-B and fig. 10 can be used to output heat maps of different performance indicators across the previously described design space of rated output power and rpm. In order to aid comparisons to actual turboprops, the aircraft sampled in section III are superimposed on these results. Some of the motors designed are going to be verified using FEM analysis. These motors are also indicated on the same diagrams.

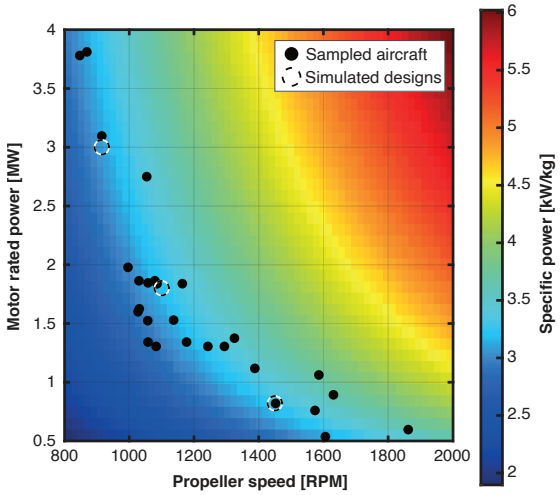

Figure 13: Analytically calculated specific power superimposed with sampled and simulated motor ratings.

Table XIV:
Performance analysis parameters

Parameter	*Value range*	*Number of steps*
J	20-100 %	20
N_r	100–125%	5

Figure 13 presents the specific power of analytically designed PMSMs. The design space comprises specific powers of 2–6 kW/kg. However, the turboprop data indicate that designed motors correspond to aircraft motors in the range of 2.8–3.7 kW/kg. Numerical information about the circled designs in fig. 13 is also shown in tables XV to XVII.

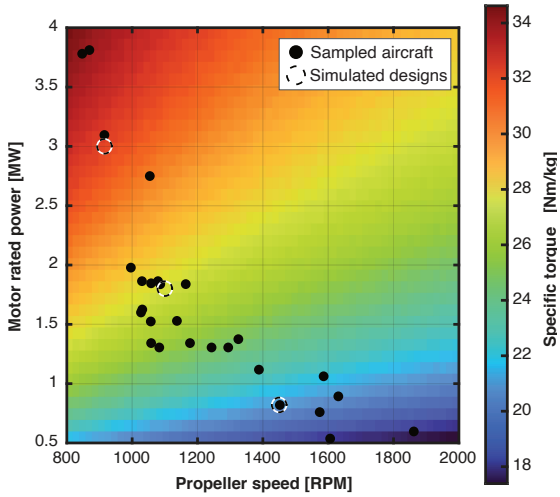

Figure 14: Analytically calculated specific torque superimposed with sampled and simulated motor ratings.

Figure 14 presents specific motor torque as a function of rated speed and power. Specific torque increases from high-speed–low-power to low-speed–high-power motors, with aircraft data points spanning the same diagonal.

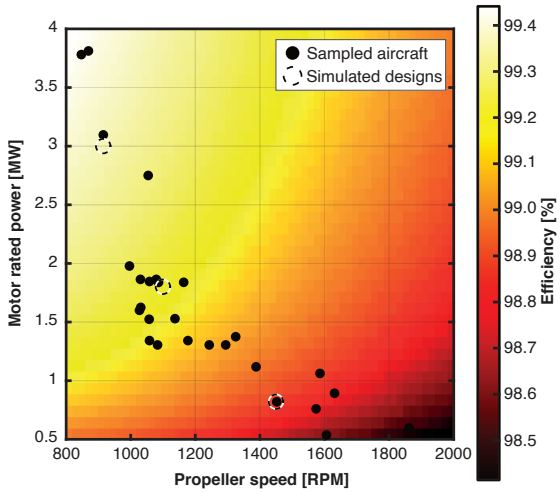

Figure 15: Analytically calculated efficiency superimposed with sampled and simulated motor ratings.

Lastly, efficiency calculations for the design space are made. The results from this is shown in fig. 15, with efficiencies between 99.4 and 98.4%. Spesific numerical data from the circled points in fig. 15 is shown in tables XV to XVII

B. FEM analysis

1) Simulation of Initial Designs: The motor designs indicated by the circled areas in figs. 13 to 15 are simulated

using a FEM analysis in COMSOL. The results from these three simulations are shown in tables XV to XVII.

2) Manual optimization: The initial sweep of the manual optimization procedure outputs motor characteristics as a function of changing tooth height. The procedure is repeated for the three selected motors of 0.82, 1.8 and 3.0 MW. Tooth length and current density are changed inversely, ensuring constant power output.

The efficiency of motors as a function of changing tooth length at their rated power and speed are shown in fig. 16a, with both initial and improved designs indicated. Similarly, specific power is also plotted for all three motors in fig. 16b. Tooth length variation significantly impacts current density, which is why current density in these cases is indicated along the x-axis.

All three motor designs have their teeth reduced in length to reach a current density of 6.5 A/mm^2. The changes in the new motor performance are shown in tables XV to XVII.

The second step of the manual optimization algorithm is to examine the effect of a changing magnet thickness. Results of this sweep are shown in figs. 17a and 17b, where efficiency increases with a reducing rate, and specific power decreases linearly as a function of magnet thickness. No immediate improvement in magnet width is found, and designs from the previous step are not altered.

Table XV:
Design output for P_r= 820-kW, N_r=1450-rpm.
A) Base analytical, B) Base Numerical,
C) Optimized h_{us}, D) Optimized h_{yr}, h_{ys}, w_{tt}

	M_{tot} [kg]	D_{es} [cm]	P_r/M_{tot}	η [%]	T_r/M_{tot}
A)	252.43	73.42	3.25 kW/kg	98.88	21.39 Nm/kg
B)	253.04	73.46	3.24 kW/kg	98.26	21.34 Nm/kg
C)*	232.19	72.33	3.53 kW/kg	98.29	23.26 Nm/kg
D)	——	——	—— kW/kg	——	—— Nm/kg

*Optimal design

Table XVI:
Design output for P_r= 1.8-MW, N_r=1100-rpm.
A) Base analytical B) Base Numerical,
C) Optimized h_{us}, D) Optimized h_{yr}, h_{ys}, w_{tt}

	M_{tot} [kg]	D_{es} [cm]	P_r/M_{tot}	η [%]	T_r/M_{tot}
A)	566.76	100.11	3.18 kW/kg	99.21	27.63 Nm/kg
B)	566.11	100.10	3.18 kW/kg	98.63	27.61 Nm/kg
C)	518.21	98.75	3.47 kW/kg	98.61	30.16 Nm/kg
D)*	517.81	98.76	3.48 kW/kg	98.62	30.18 Nm/kg

*Optimal design

Table XVII:
Design output for P_r= 3.0-MW, N_r=915-rpm.
A) Base analytical, B) Base Numerical,
C) Optimized h_{us}, D) Optimized h_{yr}, h_{ys}, w_{tt}

	M_{tot} [kg]	D_{es} [cm]	P_r/M_{tot}	η [%]	T_r/M_{tot}
A)	975.78	123.64	3.07 kW/kg	99.36	32.09 Nm/kg
B)	975.45	123.64	3.08 kW/kg	98.72	32.10 Nm/kg
C)*	900.10	122.27	3.33 kW/kg	98.68	34.79 Nm/kg
D)	902.29	122.34	3.32 kW/kg	98.69	34.70 Nm/kg

*Optimal design

The third step of the manual optimization is conducted for all motors. Improvements, however, are only attempted on the 1.8 MW and the 3.0 MW motor, and diagrams are, therefore, only presented for these motors in section V-B2. Flux density for the three measurement points as a function of either h_{yr}, h_{ys} and w_{tt} are shown for both motors.

The 1.8 MW motor has its stator yoke thickness increased by 104%, resulting in stator teeth and back iron flux density being equal. This design is indicated by the red circle in fig. 18a. This adjustment decreases the required current density, meaning tooth height can be reduced to ensure a current density of 6.5 A/mm^2 at rated power. The performance result of this scaling is shown in table XVI.

The 3.0 MW motor is subjected to a similar 104% increase in stator yoke thickness as the 1.8 MW Motor, which results in a balance in tooth and back iron maximum flux density. The motor efficiency is slightly higher than the previous design iteration; however, the mass increased. This design iteration is discarded, and its previous iteration is selected as the finalized design of the 3.0 MW machine.

3) Flight Profile Performance: The efficiency of the manually optimized motor designs is calculated as a function of output power loading and rpm. The results of this is presented in figs. 19a to 19c, together with the flight profile performance demands from fig. 5. Additionally, possible operating points for the aircraft during these flight phases are superimposed on the figures.

VI. Discussion

The main goal of this thesis is to investigate a design space of direct drive PMSMs across a span of performance demands set by modern aircraft, with electric motor designs developed to maximize viability. The design space analysis seeks to draw conclusions from these findings—which aircraft show the best potential for retrofit, trends in motor performance, and what the findings can suggest about propulsion design in electric aircraft.

Aircraft data is collected across a large span of performance demands, resulting in a design space covering power and rpm between 0.5–4 MW and 800–2000 rpm, respectively. It is found that these aircraft follow a clear trend, with power rating reducing with a negative-exponential proportionality to calculated rpm. Passenger capacity also reduces with power rating. These trends make it easier to identify motor designs that fit aircraft of a specific size bracket.

Using an analytical design algorithm makes it possible to quickly generate motor geometries for the power–rpm plane, enabling an analysis of designs related to aircraft with similar demands.

Observing fig. 13, it becomes apparent that the specific power of direct drive PMSMs remains consistent regardless of the aircraft motor rating. This consistency indicates that little gains can be achieved by electrifying a specific

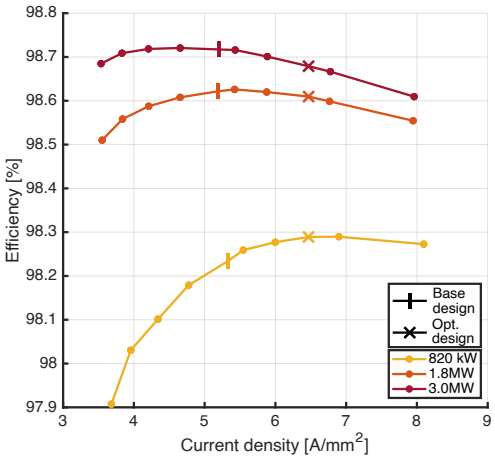

(a) Efficiency and current density.

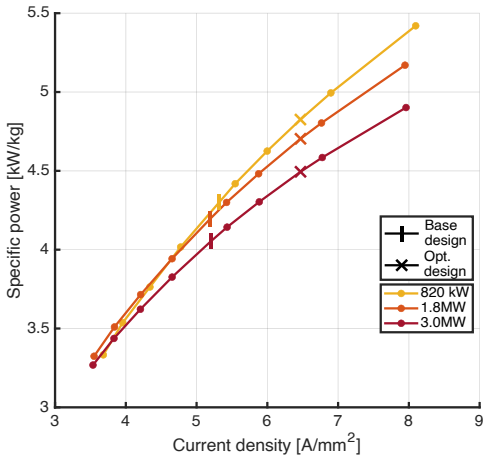

(b) Specific power and current density excluding M_{sh} and M_{enc}.

Figure 16: Results of FEM simulations as a function of reduced h_{us}/increased J for three motors.

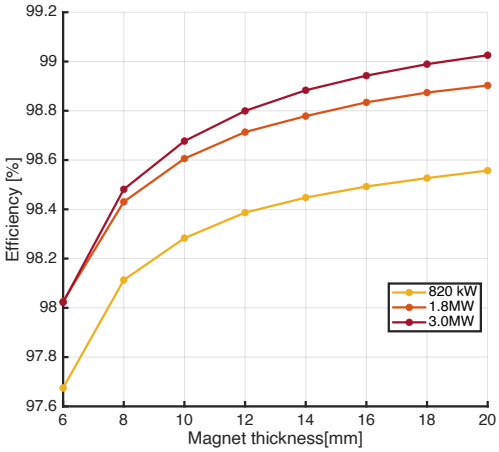

(a) Efficiency and current density.

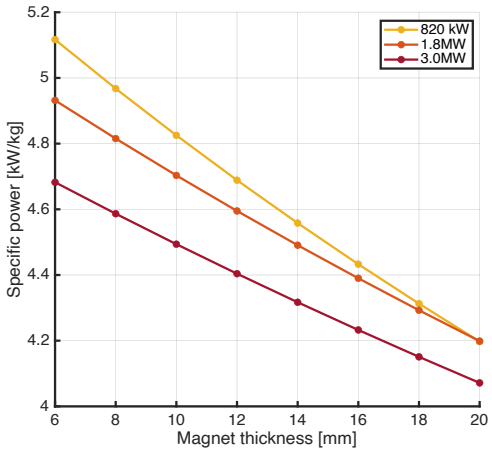

(b) Specific power and current density excluding M_{sh} and M_{enc}.

Figure 17: Results of FEM simulations as a function of increasing l_m/decreasing J for three motors.

aircraft in terms of motor mass. However, a slight increase in specific power can still be found in smaller aircraft.

The data suggest that when choosing a motor for a specific power output, selecting a smaller diameter propeller with higher RPM and constant power output can increase the specific power of the motor. However, from eq. (5), it can be deduced that this may lead to reduced propulsive efficiency. The specific power benefit of higher rpm is also reduced with decreasing power rating, meaning smaller aircraft has a minor relative reduction in motor mass if a smaller propeller is chosen.

The increase in specific power is predictable based on eq. (16). The equation indicates that geometrical size is proportional to torque so that increasing rotational velocity does not come with added mass. However, the higher rpm leads to higher f_{el}, and thus increased motor losses per eqs. (6) and (42). This loss in efficiency is stacked on top of the expected reduction in propeller efficiency.

Specific torque does not, however, remain consistent across the sampled aircraft, as shown in fig. 14. High specific torque is a feature of larger motors. The relation between output power and rpm in eq. (1) dictates that increased rpm leads to a linear reduction in torque, while increased power demand does the opposite.

From eq. (16) it is known that torque and volume are proportional $L_{cr} \cdot D_{ag}^2$, and thus at least rotor mass. If the relation of torque to mass described in this equation is purely linear, no increase in specific torque should be seen in fig. 14 due to the two terms canceling out in the calculation of specific torque. Torque increases more quickly than weight, which may be caused by increased current density or a nonlinear proportionality in stator geometry.

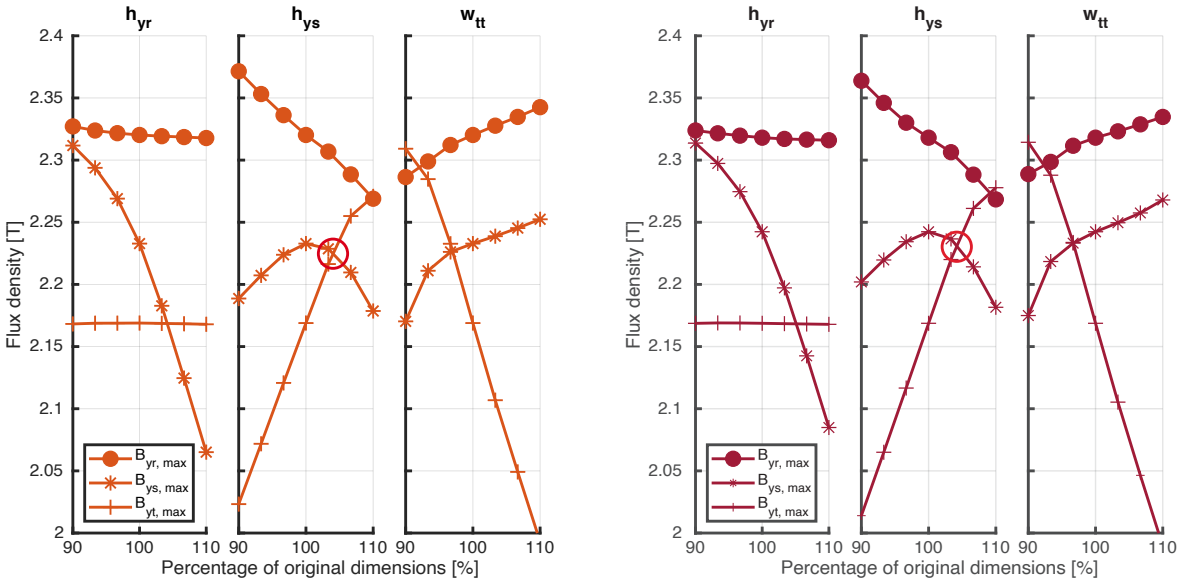

(a) $P_r = 1.8$ MW (b) $P_r = 3.0$ MW

Figure 18: Results of FEM simulations. Maximum flux density in different irons as a function iron dimensions for two motors. Selected design alteration is circled in red.

Figure 15 shows motor efficiency across the design space. Since all designs have similar current density constraints, it can be assumed that the change in efficiency is caused by a reduction in relative magnetic losses as motor rating increases. It is clear from the analytical calculations that larger aircraft benefit from higher efficiency, meaning larger aircraft may have an advantage in relative battery capacity.

Finalized motor designs are simulated across a performance space defined by the flight cycle requirements of aircraft with corresponding engine size.

During take-off, the largest power demand takes place simultaneously with increased rpm. This means that actual torque load is lower than 100%, which can be traced in figs. 19a to 19c to be between 80-90% of full torque. Efficiency at take-off remains close to the calculated rated efficiency for all motors.

When climbing, output power is reduced, and gradually decreases from 100% to around 65% of rated power, seen in figs. 5 and 19a to 19c. Sources describing how output power is reduced concerning rpm are not found, so if rpm is immediately reduced to cruise/rated rpm or this is done gradually is not known. In either case, efficiency gradually increases with the power decrease. According to fig. 5, the climb phase requires a significant portion of the aircraft total energy consumption, depending on cruise length, of course. Therefore, it can safely be regarded as advantageous that efficiency increases during the climb.

During cruise—often the longest flight phase—efficiency approaches its peak. From figs. 19a to 19c it is evident that peak efficiency is reached at lower output power for larger motors. This shift indicates that smaller motors are closer to maximum efficiency during cruise. However, since high-power motors generally seem to have higher efficiency, absolute efficiency is highest during cruise for larger motors.

In the approach and landing phase, the motors designed in this thesis are at their most efficient. However, as the amount of power required during this phase is relatively small compared to climb and cruise, the energy savings of this operational phase is smaller than for other flight phases.

It may be beneficial to move the operating point of highest efficiency to a higher power output point to facilitate optimal efficiency during cruise—the flight phase requiring the most significant amount of energy. One way to achieve this is to increase iron thickness so that the knee-point value of the B–H curve in the iron material is reached at the 65% power required during cruise. The viability of this method is supported by the three simulated motors having decreasing iron flux with a lower power rating, and that the most efficient operating point for the three motors increases with reduced power rating.

The cost of moving the point of optimal efficiency upwards in figs. 19a to 19c is however added weight. The decision must be made based on a balance in battery weight and motor weight, which is outside the scope of this thesis.

A. *Impact*

The completed electric motor designs can now be compared to the turbine motors they are made to emulate and be placed in the context of the aircraft they are designed for.

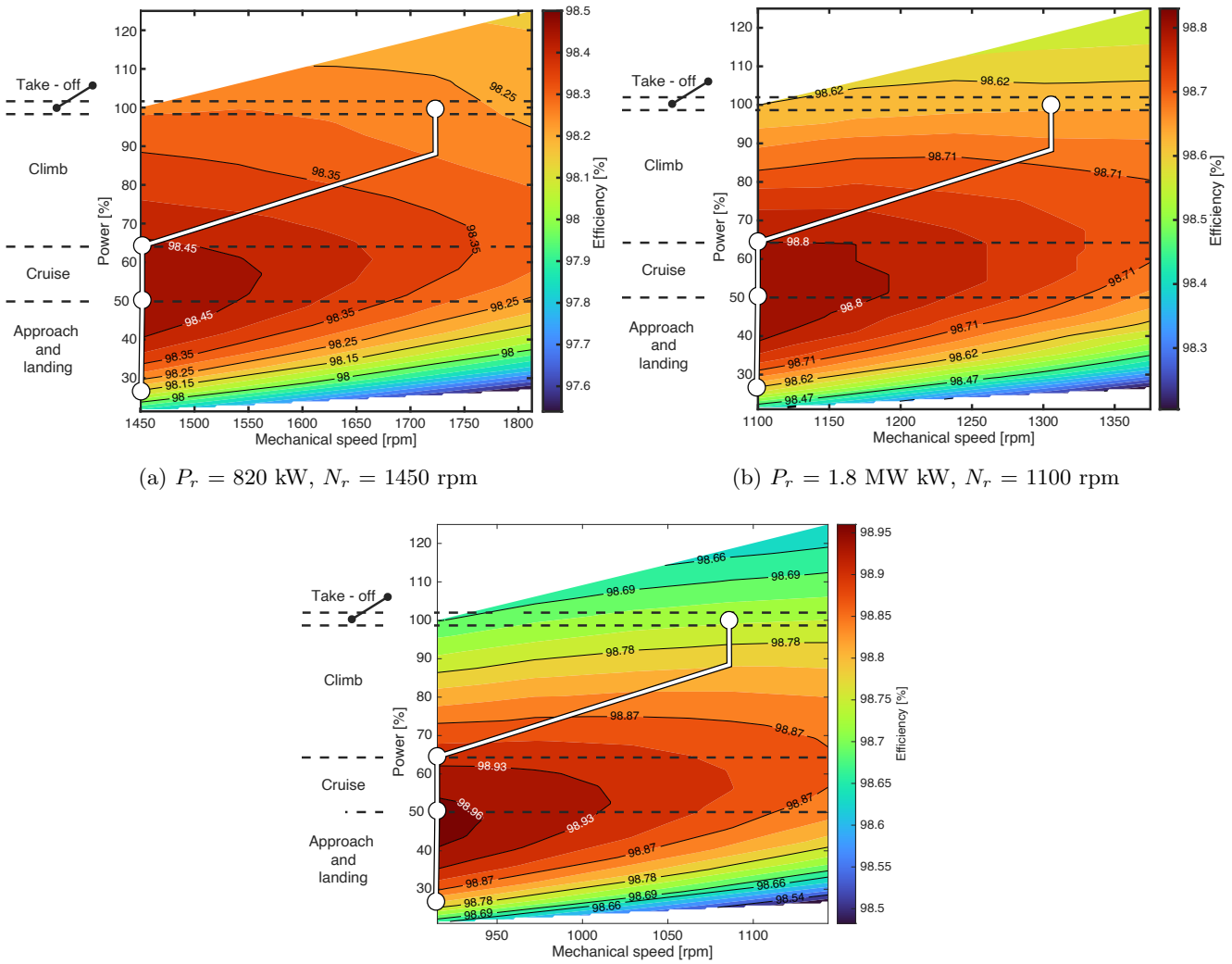

(a) $P_r = 820$ kW, $N_r = 1450$ rpm

(b) $P_r = 1.8$ MW kW, $N_r = 1100$ rpm

(c) $P_r = 3.0$ MW kW, $N_r = 915$ rpm

Figure 19: Performance characteristic of three motors during main flight phases.

This analysis will be conducted for the three excerpted electric motors—with power ratings of 820 kW, 1.8 MW, and 3.0 MW—and conceptualized with aircraft having similar power and rpm requirements.

Table XVIII presents the motor weight of electric motors compared to turbine turbines with similar speed and power. The turbine motors require reduction gearboxes that are included in the presented turbine engine weights. For the smaller motor, the electric power unit is 158 kg lighter than its turbine counterpart. This trend shifts gradually as motor size increases, and for the largest motors, the electric alternative is 200 kg heavier. The trend in fig. 13 where power density remains constant is therefore not the case for the sampled turbine motors, which improve with size in terms of specific power. In terms of retrofitability, larger aircraft may require reinforcements to handle the relatively heavier electric motors.

Retrofitting electrical motors means a replacement of the entire propulsion system. Mass calculations regarding

Table XVIII:
Electric motor/turbine weight comparison for three orders of motor ratings.

Engine	(Dry) Weight	Source
PW 118	390.5 kg	[71]
820 kW PMSM	232.19 kg	—
PW125B	480.8 kg	[71]
1.8 MW PMSM	517.81	—
R-R AE 2100P	700 kg	[39]
3.0 MW PMSM	900.10 kg	—

the weight of this system with components like electrical converters or fuel pumps for electric and turbine propulsion, respectively, are not conducted. This makes a comparison of total system weight difficult.

An evaluation of motor volume can be made based on calculated geometric parameters. As volume is not among the optimization variables directly, an in-depth analysis is not made. The three PMSMs are presented together with propellers for aircraft with similar performance demands

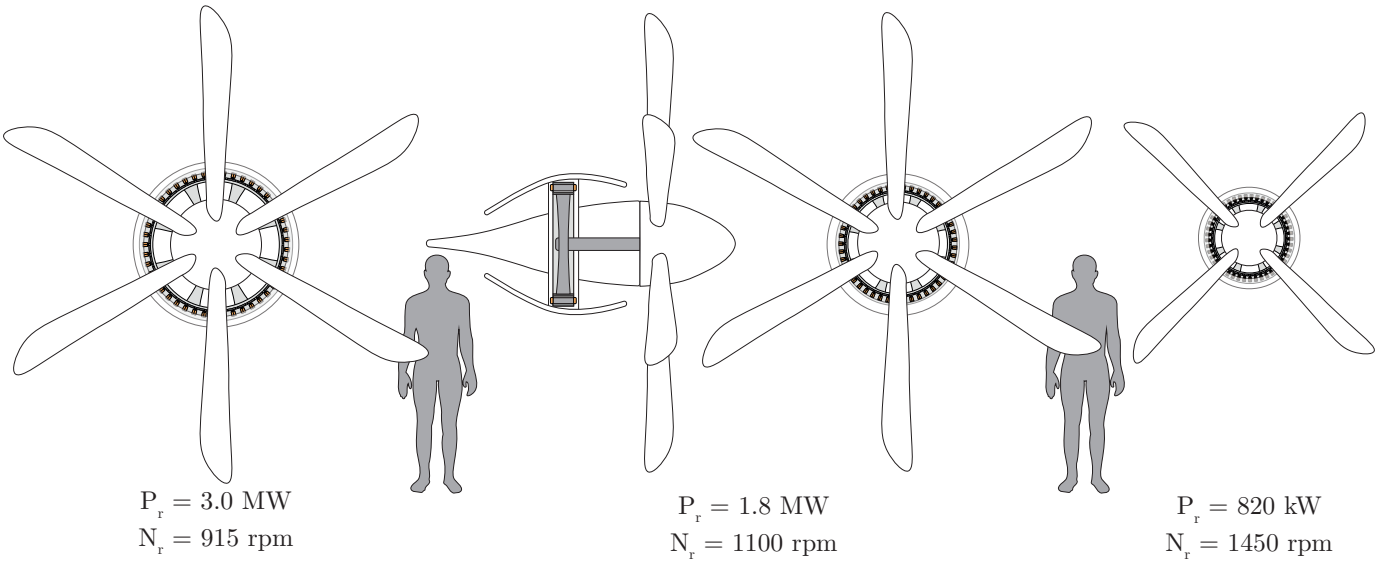

Figure 20: Motor designs together with propellers from similarly performing aircraft.
Right to left: Saab 2000, Fokker 50, Metro 23.

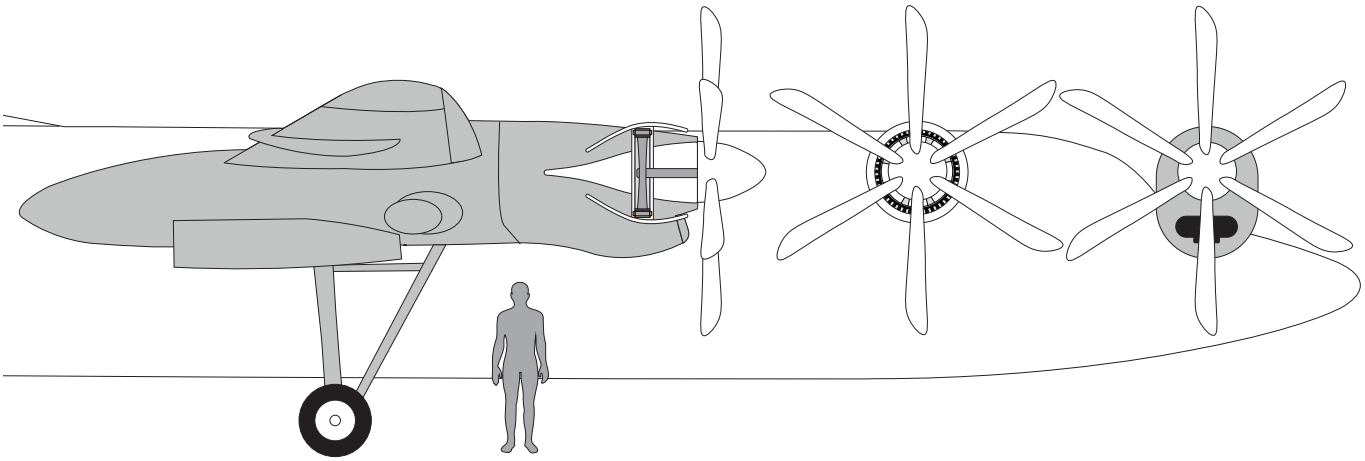

Figure 21: Fokker 50 compared to 1.8 MW PMSM design. Aircraft schematic adapted from Marcusroos [70].

in fig. 20. A simple nacelle structure is included in the sketches to provide context.

The diameter dictated by the selected aspect ratio is in all cases larger than the propeller hub diameter, which is seen in fig. 20. The diameter is comparatively similar to those of turboprop aircraft nacelles, and the diameter can therefore be considered feasible. The electric motor length is much shorter than that of turbo motors, indicating that the electric motor volume is smaller. This claim is supported by comparing the 1.8 MW motor to the engine nacelle of the Fokker 50 —an aircraft with similar performance—in fig. 21. Only the front part of the nacelle holds the turbo motor, while the aft section holds the landing gear assembly. The designed motor fits within the original nacelle, albeit with a higher weight.

As the electric motors increase in rated output power, their diameter relative to their propeller diameter increases. This trend is caused by the diameter of propellers remaining relatively constant compared to increased power rating. The result of this is that larger motors are more susceptible to problems regarding drag and other diameter-based constrains.

Due to the efficiency dynamic shown in figs. 19a to 19c, some tweaks to aircraft performance could be made to improve total energy economy, thus reducing energy storage requirements. If possible, the climb phase could be extended, reducing power output closer to optimal efficiency. It is assumed that cruise power output cannot be reduced. To improve efficiency in this flight phase, the optimal operation point for the motors can be modified according to the previous discussion.

According to the analytical design space and the performance maps, larger motors are better in terms of efficiency and specific torque. However, specific power is slightly

lower, and the large motors are also comparatively heavier than their turbo motor counterparts. If the motor mass is considered the main issue, smaller aircraft may be easier to electrify. However, since batteries can be considered a significant part of the total aircraft mass in fully electric aircraft, electrifying larger aircraft may yield a relative net reduction in system mass due to their higher efficiency.

Since regulatory and system-related concerns are not addressed in the motor dimensioning procedures, these matters are not up for discussion and may speak in favor of distributed propulsion. Distributed propulsion can, for example, have lower voltage levels, as they employ smaller motors. This may reduce the size of insulation, power electronics or other weight-dependent technology. Multiple motors may also cause a higher system reliability, since a single motor failure leads to a smaller thrust loss with more motors.

The findings in this thesis indicate that distributed propulsion does not yield gains in specific motor weight or efficiency from a purely motor perspective. The findings indicate that the optimal choice in direct drive propulsion is having a few large motors and not several smaller ones. Since specific power remains constant, replacing one motor with two of half the power rating only leads to efficiency reduction.

B. Aircraft Data

The aircraft data collection is done to ensure that representative aircraft for the entire range of commercial turboprop aircraft are represented. For the larger aircraft, the Dash-8-Q400, the ATR-42, and the ATR-72 are some of the most common [72]. For smaller turboprop aircraft, the selection of sample aircraft is made while making sure motors of different sizes are represented through sources like Jackson [39]. Based on these considerations, the selection of aircraft is deemed representative of the current fleet of turboprop aircraft.

Larger turboprops than the sampled 70+ passenger aircraft exist but are classified as military. Motor ratings far above 4 MW occur, e.g., the Atlas A400, which has four 8 MW turboprops [73]. Military turboprop aircraft have—in particular—lower propulsive efficiency than their civilian counterparts, primarily due to their higher operating speeds. The contrasting performance characteristics of these aircraft are large enough that they are considered inapplicable for use as comparisons in this thesis.

The aircraft data presented in table II is based on online sources; however, due to difficulties finding propeller rotational velocities during cruise, this data has to be approximated. The performance of the sampled aircraft varies greatly, and the basic assumption that a propeller tip speed typically holds a speed of Mach 0.8 must be verified.

According to Farokhi [6], advanced turboprops can reach tip speeds of up to Mach 1.3, with cruise speeds between Mach 0.7 and 0.8. However, this is only the case for advanced turboprops, with more typical aircraft cruising around Mach 0.4–0.6. Since the last two Mach numbers correspond to speeds between 130–200 m/s, table II indicates that the sampled aircraft typically cruise within this envelope. Therefore, it is reasonable to assume that the sampled civilian aircraft do not reach the tip speeds up to Mach 1.3.

Assuming identical cruise height for all aircraft is a simplification, but the selected altitude is within the expected cruise envelope of the sampled aircraft. A tip Mach number of 0.8 is assumed for all aircraft, making propeller tips subsonic at a cruise altitude of 13 000 ft. This assumption is based partly on the expectation that the higher efficiency of subsonic tips is desirable and comparisons to empirical data.

Propeller operating ranges are gathered for some aircraft and compiled in table XIX to verify the calculated propeller rpm. Three aircraft are selected to represent different airspeeds.

The Dash-8-Q400, rated at a comparatively high airspeed to other aircraft, has a typical propeller speed of 850 rpm [16, 36], corresponding closely to the calculated value. A second cruise RPM is found for the Dash-8-100A—1050 rpm. This result is also close to the approximation. The LET L-410 UVP-E20, however, is not as close to the approximation and has a propeller cruise speed of 1700 compared to the calculated value of 1862 rpm.

Based on the abovementioned considerations, the approximated rpm values are deemed sufficiently accurate for further work, although the results may be less accurate for the slowest moving aircraft.

C. Initial Design Decisions

The choices made in advance of the analytical design procedure and succeeding motor designs lead to consequences for the final result. This subsection will discuss the impact of these assumptions.

The design space that lays the foundation for most results gathered in this thesis is based on motors designed for rated maximum motor output power and propeller rotational velocities corresponding to medium to low rpm approximations. This results in the electric motors never operating at the operating point they are designed for. The only maximum power demand occurs during take-off, in which

Table XIX:
Calculated versus actual propeller rpm of aircraft.

Aircraft	**Calculated**	**Cruise**	**Max**
Dash-8-Q400 [16]	847 rpm	850 rpm	1020rpm
Dash 8-100A [18]	1057 rpm	1050 rpm	1100 rpm
LET L-410 [19]	1862 rpm	1700 rpm	2080 rpm

case propeller speed is increased above the rated motor speeds.

Because iron core saturation in the motors is higher than initially designed for (according to FEM-simulated motor data), designing the motors for the full power output requirement yields both efficiency and weight improvements. Ideally, efficiency should be highest at the most utilized operating point during a flight, as is the case. A yoke flux density of the initial 1.85 T at rated operation would result in more significant rotor iron than is necessary. The motor approaching magnetic saturation during maximum power is, therefore, beneficial. In addition, the fact that efficiency increases until ≈50% of maximum power causes the cruise phase to have close to optimum efficiency.

Suppose the analytical algorithm is updated to improve stator flux approximation. Then, instead of selecting the knee point flux density as the desired value, a flux density value approaching saturation should be used to reduce iron mass.

The electric motors are designed for a specific operating point, and a wide speed performance in the motors is not investigated. This narrow analysis means that the field weakening characteristic of the motors is not analyzed. This choice is, however, justified, as the narrow rpm envelope of fixed speed propellers deems the need for field weakening unnecessary [17].

The motor aspect ratio, λ, is selected to be 0.2 to maximize efficiency. It is possible to retain the torque rating of the motor while increasing λ by preserving the product of $D_{ag}^2 \cdot L_{cr}$ per eq. (16). As previously stated, this may lead to a reduction in specific power and efficiency, but with the benefit of reduced volume [50]. A barrel-shaped motor would more closely resemble the aspect ratio of a turbine motor better than a disc-shaped one. Therefore, a higher aspect ratio could still have relevance in this regard.

Some technologies could improve performance that is not considered in this thesis. At the architecture level, the implementation of a Halbach-rotor may come with improved specific power improvements. A Halbach array uses magnets polarized in gradually rotating directions, leading to all flux being conducted through the magnets, eliminating or reducing the need for rotor iron, thus reducing weight. Additionally, magnetization length increases, effectively increasing magnet thickness without expanding the motor diameter. This could lead to reduced current demand, either reducing the required slot size and mass, or increasing efficiency.

A limiting factor of the analysis is the number of design parameters that remained constant throughout the design procedure. Pole count, slot count, air gap thickness, and tooth geometry are constant. Including these parameters in the optimization procedure may have led to improved performance.

The slot fill factor value may be lower than what is reasonable to assume, as it implies that 90% of the slot area for each coil in the double slot can be utilized. According to Alderks [74], advanced windings can have fill factors of 70–80%, with some manufacturers claiming 85% [75]. The intended motor design is also meant to employ liquid cooling, which could further reduce the available slot area. Therefore, it can be determined that the selected slot fill factor equating to 90% of the entire slot area is too high. Correcting for this would increase slot area by elongating teeth which would cause the total mass to increase.

Since all motors are impacted, it can be assumed that this correction would lead to specific power reducing evenly across the design space in fig. 13. Repeating the analytical design algorithm with a slot fill factor of 37.5%, equating to a total fill factor of 75%, leads specific power to be reduced by 4.2% for an electric motor previously with a specific power of 3.04. This change is reflected in values across the design space and is smaller than the specific power gain attained by manual optimization. The change is therefore not considered to cause significant changes in the results.

It is elected to include an approximated motor enclosure mass in the motor mass calculations during the initial design process. This inclusion creates a more realistic depiction of the motor-design weight but adds a level of uncertainty. However, because data weight distribution in current aeronautical electric motors is unavailable, the assumption is maintained and based on an automotive motor.

The remaining choices are based mainly on literature, and the considerations made can be seen in section IV-A. The design variable choices are considered satisfactory.

D. Analytical Dimensioning

1) Algorithm: Generation of the motor design space is conducted by using constraints on iron flux density and thermal loading in the stator slots. Evaluation of these parameters could have been conducted through numerical means, i.e., by simulating motor dimensions iteratively in software like COMSOL to attain magnetic and thermal loading values. This method, however, is computationally intensive and unviable for an algorithm requiring as many iterations as the one employed. By using the analytical equations described in section II-C, the algorithm can produce enough motor designs to present a comprehensive and nuanced design space as presented in figs. 13 to 15.

The algorithm iteratively scales the rotor iron to achieve satisfactory flux density and thermal loading. Since the same parameter—D_{er}—is used to achieve designs adhering to the constraints, in a scenario where, for instance, flux density falls below maximum values long before thermal loading, parts of the motor to be over-dimensioned regarding flux density. However, gradually increasing the rotor inner diameter and selecting the least massive design mitigates this issue. The least massive design occurs when

tolerable flux density and thermal loading are achieved simultaneously. The double constraints of the inner loop are therefore not considered problematic in the sizing procedure.

Analytically evaluating constraints is based on more simplifications than numerical simulation. The data must therefore be validated, which is done using FEM in COMSOL, which will be further discussed in section VI-F.

2) Simplifications: Simplifications are made in the analytical design algorithm that impacts the end results. The loss calculation is incomplete, negating several kinds of losses. Efficiency can therefore be assumed to be lower than shown in fig. 15. A more complete loss simulation is conducted in the FEM analysis, which will be discussed in section VI-F.

Rotor iron loss is calculated using electrical frequency, but since the rotor iron never experiences reversing magnetic fields, both frequency and amplitude are different from the values used. In reality, rotor core losses can be assumed to be lower than those calculated. The impact of this is limited since rotor iron makes up a significantly smaller portion of iron mass than the stator.

Motor temperature is not modeled during the analytical procedure. It is therefore assumed that cooling can keep materials at 60°C as stated in the chosen design parameters. Higher temperatures will increase current losses as copper resistivity rises with material temperature. The permanent magnets are also more susceptible to demagnetization at higher temperatures. However, the Curie temperature of the selected magnet grade, N52M, 300°C is much higher than the selected operating temperature.

An improvement in motor iron flux density calculation could be made, which becomes clear when comparing analytically and numerically attained flux density. This could be achieved by modelling flux linkage with stator coils in the analytical equations

E. FEM simulation

1) Simulation: The simulation conducted using FEM-analysis in COMSOL has some idiosyncrasies that may impact the final result.

In order to approximate motor iron losses, a curve fitting tool—together with material-specific data sheet values—is used to approximate the equation constants. The resulting curve-fit goodness parameters are shown in table X and show that the loss approximation may not be as accurate as could be desired. However, since the R-square value is 98.35%, the loss calculation can be considered accurate enough for its purpose.

During the curve fitting, the anomalous loss constant K_{an} is bound at its non-zero constraint, effectively rendering anomalous losses negated. These losses are typically small, and it is, therefore, determined that this negation is acceptable [26].

The choice of loss calculation is made based on data availability. If more data points are made available for the selected stator material, more advanced loss calculations could be conducted for motor iron, e.g., CAL2 [76].

Electrical dimensioning is conducted during the simulation process by keeping a constant turn number and varying current density to achieve rated power. The three motors of 820kW, 1.8 MW, and 3.0 MW thus have maximum voltage levels of 1.3, 2.1, and 2.8 kV, respectively. These voltage levels are high compared to the voltage levels used in current aircraft, but within the range of some concepts with engine supply up between 1 kV to 10 kV DC [77, 47, 78]. Voltage can be reduced to fit within constraints by increasing the number of turns; however, this would lead to increased currents, larger slots, and increased weight.

2) Simplifications: Just as with the analytical design algorithm, the FEM analysis is subjected to simplifications impacting the simulation results.

Temperature changes are not modeled in COMSOL, and a temperature of 60 °C is used as a constant material temperature as with the analytical investigation. In the same vein, this will cause simulated copper losses to be lower than if the motor had an increasing temperature.

Rotor loss calculation is based on electric frequency in COMSOL. Since the rotor flux remains relatively constant compared to stator flux, rotor losses are overstated in COMSOL in the same way they are in the analytical results.

The impacts of any COMSOL model simplifications are considered acceptable and do not impact final results in any way that would change conclusions.

F. Analytical Result Verification

1) Base Design: The initial FEM analysis is conducted on a selection of output geometries from the designs in figs. 13 to 15. The specific results for each of the three designs discussed in this subsection are found in tables XV to XVII. Additional results that will be discussed in this section can be found in appendix B.

It is found that both specific torque and specific power are identical or nearly identical when simulated using a numerical method for all three motors. These parameters are expected to be identical because they only depend on input geometry and power rating. Differences in the geometric design must cause the reason for the discrepancy.

Even though the parameters governing the overall dimensions of the motors are identical, some simplifications are made when calculating mass analytically. The COMSOL model has a more advanced design than what is accounted for in the analytical equation, with rounded shoe tips. The discrepancy is, however, small and is therefore considered negligible. It can therefore be determined that figs. 13 and 14 are valid depictions of the motor designs.

A more significant discrepancy can be found in approximated efficiency for the three designs compared to analytically calculated values. Losses are 55%, 73%, and 100% larger for the 820 kW, 1.8 MW, and 3.0 MW motors, respectively. As discussed in section VI-D2, the analytical analysis only calculates iron and copper losses, while magnet eddy current losses are additionally included in FEM calculations. Magnet eddy current losses account for 4.2%, 10.8%, and 19.6% of the total losses during the simulation and can thus explain parts of the increase in discrepancy between the three motors.

The disregard for magnet eddy current losses in the analytical model can only explain parts of the loss discrepancy between analytical and numerical analysis. During the analytical dimensioning process, a flux density of 1.85 T, the knee point of the iron material, is used to dimension the iron air gap flux calculated from magnet remanence. It is this flux density that is later used to approximate magnetization losses. The FEM simulations show that iron flux density is understated and that stator flux density is in the range of 2.16–2.25 T. If a flux density of 2.2 T is used in place of the design parameter of 1.85 T in eq. (40), the differences in losses are reduced to 0%, 15%, and 21% for the three respective motors. This indicates that most of the loss discrepancy is caused by the different flux densities.

The remaining loss calculation differences may be caused by the two iron loss equations used: Steinmetz for the analytical simulation and Bertotti for the numerical evaluation.

The main weakness of the analytical algorithm thus lies in its loss calculation. The main inaccuracy stems from inaccurate flux density estimation. This can be expected to be the case, as a significant benefit of FEM analysis is its ability to simulate magnetic fields. The fact that loss discrepancy increases with motor size will mean that both the absolute and relative accuracy of fig. 15 is impacted. One can assume that efficiency across the illustration should be reduced and that motors of higher power ratings are impacted more. However, since the three motor designs simulated still exhibit increasing efficiency in tables XV to XVII, it can be assumed that the trend of high-power–low-rpm motors being more efficient is still apparent.

2) Design improvements: The first step in the manual design procedure is to change motor tooth length. This is conducted by shortening stator teeth, reducing both tooth weight, winding weight, and back-iron weight due to the smaller motor radius. Based on Pyrhönen et al. [48], the initial assumption of 4.9 A/mm^2 in current density is determined to be increased to 6.5 A/mm^2. Since the iron cross-section in the flux direction is not changed, flux density remains constant, as is seen.

From fig. 16 the difference in the efficiency and specific power of the three motors becomes apparent.

The smaller the motors have a disproportionately lower efficiency based on the change in power rating between them, as seen in fig. 16a. It also becomes clear that each motor design has an optimum tooth length. Since flux density remains constant, added mass through tooth elongation leads to a significant iron loss increase. Therefore, optimal tooth length occurs where both currents are low enough not to cause excessive coil loss, and the amount of motor iron is not so significant as to produce excessive iron losses. Selecting the current density to 6.5 J/mm^2 has resulted in motors close to this peak for all three designs.

Figure 16b illustrates that the relative difference in motor specific power increases with the increased current loading, suggesting that if the motors in fig. 13 increased their power output, the similarity in specific power could diverge.

The next step of the manual optimization method is to investigate the impact of changing magnet thickness on motor performance. As can be seen in figs. 17a and 17b, increasing thickness causes an increase in efficiency and a reduction in specific power.

The cause for the efficiency increase is that coils and their associated losses produce a smaller portion of the motor flux—specific power increases, which is a natural consequence of increasing magnet thickness and motor diameter.

Although it is reasonable to assume that each power requirement has a different optimal magnet thickness as the optimal choice, no design alterations are made based on this sweep analysis. The reason behind this decision is that efficiency and power density must be actively traded at the cost of each other, a judgment previously decided to keep outside the scope of the thesis.

The reduced current density demanded of motors with increased magnet thickness could cause reductions in the slot area, equating to an overall reduction in motor mass even though magnet size is increased. However, the complexity of this type of iterative optimization is demanding in simulation time and is not conducted.

It is decided to balance the stator tooth and back-iron flux density to increase motor iron utilization. Rotor iron flux density is generally higher and is chosen not to be balanced due to being separated from the stator and subjected to a different magnetization characteristic than B_{ys} and B_{th}.

It is found that for the 820 kW motor, the stator flux is satisfactorily balanced. There are no adjustments made to the design in this step. However, the sweep data is still included in appendix A.

For the 1.8 MW motor, the discrepancy in yoke flux is minimized. This balancing can be achieved by reducing tooth width or increasing stator yoke. Since copper density is higher than the magnetic iron material, it is decided to expand the stator yoke. After this adjustment is made, it is clear that the required input current is reduced. This reduction is likely due to increased flux permeability. The

subsequent reduction in current requirements leads to a secondary reduction in tooth length to keep the current density at the pre-specified level. The change in geometry is minor for these adjustments, but a slight increase in specific power and efficiency can be attained.

The 3.0 MW motor has a similar flux discrepancy to its counterpart of 1.8 MW. A similar stator yoke adjustment is conducted with a following tooth length reduction. The slight specific power benefits gained for the smaller motor design are not found when applying the alterations to the 3.0 MW motor. However, efficiency increases as expected when magnetic saturation is reduced with larger iron. Since efficiency is essentially traded for specific power, it is decided not to select this updated design for the final simulations due to the desired avoidance of exchanging motor weight for battery weight and vice versa.

It is unclear why a gain in specific power could not be achieved for the 3 MW motor design. One explanation is that the increased diameter means that expanding stator yoke contributes more relative to the total mass, which keeps the reduction in tooth length from compensating for the increase. Another explanation is that the larger of the two motors is close to a local optimum. Other parameters outside the scope of the manual optimization may then be changed to achieve performance benefits.

The manual optimization procedure leads to an improved specific power, with only slight reductions in efficiency. It is concluded that the improvements are meaningful and that the specific power density map of the design space is accurate. It is also found that specific density can be improved by around 10% with manual optimization.

3) Optimization Method: Conducting a manual optimization procedure is made to avoid lengthy simulation and excessive expansion of the project scope. However, the decision limits the number of design iterations and means that a proper optimal design is not found.

The final results are considered valid as indicators for direct drive PMSM design trends for aircraft. If an automatic optimization algorithm is implemented, more design parameters could be investigated, and better results can be found for the tweaked variables manually. However, since the amount of performance gain achieved by manual optimization is limited, it can be concluded that significant improvements are difficult to attain, even with automatic iterative optimization.

VII. Conclusion

A design space of direct drive PMSMs across a wide array of turboprop aircraft performance requirements is completed. The design space spans rated motor power in the range of 500 kW to 4 MW, with rpm in the range of 800-2000 rpm. The compilation of aircraft data requires some approximation but forms a solid foundation as input design parameters for a PMSM sizing algorithm. In order to form the design space, an analytical procedure is applied to reduce total calculation time, which allows for the generation of high fidelity heat maps of different motor performance indicators.

It is found that slight variation in specific motor power occurs across the design space, with specific power ranging between 2.8–3.7 kW/kg, with smaller motors having slightly higher specific power. Specific torque rises with motor output power, reaching 34 Nm/kg for the largest motors of 3.8 MW, with the smallest motors around 18 Nm/kg. Efficiency rises as a function of increasing motor size during the procedure.

Analytical data is verified by simulating a selection of the motor designs using FEM simulation implemented in the software COMSOL. The results indicate that loss calculation grows between 50% and 100% when simulated analytically, increasing with motor rating. This analytical understatement means that efficiency in the design space ranges between 98.7% and 98% across the design space, increasing with output power and increasing inversely with rpm.

The design algorithm is also verified by manually optimizing a selection of motor designs, where around a 10% improvement in specific power can be achieved.

Some of the motor designs are simulated during a representative flight profile. It is found that motor efficiency is improved during cruise and climb phases compared to 100% output power, a benefit in terms of energy preservation.

A comparison between some designed PMSMs and turboprop engines of similar power and speed ratings is made. It is discovered that smaller EMs are around 40% lighter, and larger motors are up to 30% heavier than their turbine motor counterparts.

The summation of results concludes that retrofit of electric motors in contemporary turboprop aircraft has better viability in larger aircraft due to increased efficiency and only slightly reduced specific power. The selection of propulsion types like distributed propulsion is found to have little gains in terms of mass, as specific power remains relatively constant across the selected design space.

VIII. Further work

A significant constraint in the design processes' ability to find optimal designs is the number of fixed variables across the specified design space. Further experimentation and variation of these initial parameters could uncover higher performance motor designs than those presented in this thesis. Expanding the analytical algorithm to include technologies like a Halbach array could also reveal further enhancements.

The analytical design algorithm could be improved to yield more accurate results, especially in terms of loss

calculation. The most significant grievance in this regard is the algorithm's inability to model armature reaction and, therefore, under-dimensioning motor iron for the desired flux density.

Repeating the FEM-based analysis by optimizing the motor designs automatically by applying methods like pattern search could lead to Pareto-optimal motor designs. This would also require the implementation of an objective function weighting performance factors like efficiency and specific power. The results from this analysis could be used to adjust the analytical algorithm and improve the validity of the entire design space.

This thesis could expand to other propulsion methods than conventional propellers, like the faster spinning fans used in turbofans. These fans are not fixed speed, which means the output characteristics of the motor designs in a flight phase may look different. Although less efficient, fans allow for higher airspeed and can thus lead to a higher turnover rate. The economics of these two propeller technologies could therefore be compared.

References

[1] European Commission, Directorate-General for Mobility and Transport, and Directorate-General for Research and Innovation, *Flightpath 2050 : Europe's vision for aviation : maintaining global leadership and serving society's needs*. Publications Office, 2011.

[2] S. W. Ashcraft, A. S. Padrón, K. A. Pascioni, and D. L. Huff, "Review of propulsion technologies for n+3 subsonic vehicle concepts," 2011.

[3] L. Boggero, S. Corpino, A. De Martin, G. Evangelista, M. Fioriti, and M. Sorli, "A virtual test bench of a parallel hybrid propulsion system for UAVs," *Aerospace*, vol. 6, no. 7, 2019. [Online]. Available: https://www.mdpi.com/2226-4310/6/7/77

[4] M. Henke, G. Narjes, J. Hoffmann, C. Wohlers, S. Urbanek, C. Heister, J. Steinbrink, W.-R. Canders, and B. Ponick, "Challenges and opportunities of very light high-performance electric drives for aviation," *Energies*, vol. 11, no. 2, 2018.

[5] J. O. Reimers, "Introduction of electric aviation in Norway," Green Future AS, Feasibility study, 2018.

[6] S. Farokhi, *Aircraft Propulsion*, 2nd ed. John Wiley & Sons, 2014.

[7] R. Babikian, S. Lukachko, and I. Waitz, "The historical fuel efficiency characteristics of regional aircraft from technological, operational, and cost perspectives," *Journal of Air Transport Management*, vol. 8, pp. 389–400, 11 2002.

[8] S. Doyle, "The measure of cessna ecaravan: The world's largest all-electric aircraft recently made a successful maiden flight over washington state, engine manufacturer magnix announced," *Engineering & Technology*, vol. 15, no. 7/8, pp. 92–93, 2020.

[9] F. Anton, "eaircraft: Hybrid-elektrische antriebe für luftfahrzeuge," Sep 2019.

[10] "'Spirit of Innovation' stakes claim to be the world's fastest all-electric vehicle," *Rolls-Royce–Press releases*, Nov 2021. [Online]. Available: https://www.rolls-royce.com/media/press-releases/2021/19-11-2021-spirit-of-innovation-stakes-claim-to-be-the-worlds-fastest-all-electric-vehicle.aspx

[11] A. El-Refaie and M. Osama, "High specific power electrical machines: A system perspective," in *2017 20th International Conference on Electrical Machines and Systems (ICEMS)*, 2017, pp. 1–6.

[12] *Find out more – magni350 epu and magni 650 epu*, https://www.magnix.aero/services, magniX, 11 2021, Accessed: 14 11 2021.

[13] X. Zhang, C. L. Bowman, T. C. O'Connell, and K. S. Haran, "Large electric machines for aircraft electric propulsion," *IET Electric Power Applications*, vol. 12, no. 6, pp. 767–779, Jul. 2018, publisher Copyright: © The Institution of Engineering and Technology 2018.

[14] D. Lee, T. Balachandran, N. Salk, J. Schuh, A. Yoon, P. Xiao, Y. Yu, S. Lin, P. Powell, and K. K. Haran, "Design and prototype of a high power density slotless PMSM for direct drive aircraft propulsion," in *2021*

IEEE Power and Energy Conference at Illinois (PECI), 2021, pp. 1–6.

[15] H. Broch, "PMSM characteristics for fully electric propulsion in retrofitted aircraft," Department of Electric Power Engineering Technology, NTNU – Norwegian University of Science and Technology, Project report in TET4520, Dec. 2021.

[16] "Dash 8-Q400 - power plant," Feb 2009. [Online]. Available: https://www.smartcockpit.com/docs/Q400-Power_Plant.pdf

[17] B. Jux, S. Foitzik, and M. Doppelbauer, "A standard mission profile for hybrid-electric regional aircraft based on web flight data," in *2018 IEEE International Conference on Power Electronics, Drives and Energy Systems (PEDES)*, 2018, pp. 1–6.

[18] *Type certificate data sheet for De Havilland DHC-8*, European Aviation Safety Agency, 8 2021, issue: 15.

[19] *Airplane flight manual for the L 410 UVP – E20*, LET, a.s., 05 1998.

[20] S. Vaschetto, A. Tenconi, and G. Bramerdorfer, "Sizing procedure of surface mounted PM machines for fast analytical evaluations," in *2017 IEEE International Electric Machines and Drives Conference (IEMDC)*, 2017, pp. 1–8.

[21] J. Pyrhönen, T. Jokinen, V. Hrabocová, and H. Nimelä, *3.1.1 Air Gap and Carter Factor*, 1st ed. Wiley, 2009.

[22] S. E. Skaar, O. Kroevel, and R. Nilssen, "Distribution, coil-span and winding factors for PM machines with concentrated windings," in *Proc. of Int. Conf. on Electrical Machines*, no. 306, 2006.

[23] Engineering ToolBox. Resistivity and Conductivity - Temperature Coefficients Common Materials. [Accessed: 15 12 2021]. [Online]. Available: https://www.engineeringtoolbox.com/resistivity-conductivity-d_418.html/

[24] D. Hanselman, *Brushless Permanent Magnet Motor Design*, 2nd ed. Lebanon, Ohio: Magna Physics Publishing, 2006.

[25] H. Zaw, S. Yue, and Y. Li, "Comparative core loss calculation methods for magnetic materials under harmonics effect," *IOP Conference Series: Materials Science and Engineering*, vol. 486, p. 012019, 07 2019.

[26] G. Díaz, P. Arboleya, C. Gonzalez-Moran, and J. Gómez-Aleixandre, "Revision of the hysteresis and excess loss computation method as a means of improving the rotational loss estimate in induction motors," *Electric Power Applications, IET*, vol. 1, pp. 75 – 81, 02 2007.

[27] G. Bertotti, "General properties of power losses in soft ferromagnetic materials," *IEEE Transactions on Magnetics*, vol. 24, no. 1, pp. 621–630, 1988.

[28] F. Fiorillo and A. Novikov, "An improved approach to power losses in magnetic laminations under non-sinusoidal induction waveform," *Magnetics, IEEE Transactions on*, vol. 26, pp. 2904 – 2910, 10 1990.

[29] P. Jackson, *Jane's all the World's Aircraft 2000-01*. London: Jane's Information Group, 2000.

[30] J. P. Fielding, *Introduction to aircraft design*. Cambridge University Press, 1999.

[31] "Harakteristiki AN-3," http://aviaros.narod.ru/an-3.htm, 2013, Accessed: 14 11 2021.

[32] "Factsheet ATR 72-600," https://www.atr-aircraft.com/wp-content/uploads/2020/07/Factsheets_-_ATR_72-600.pdf, 07 2020, Accessed: 14 11 2021.

[33] "De Havilland Canada DHC-8 Dash 8," https://www.baesystems.com/en/heritage/de-havilland-canada-dhc-8-dash-8, 2021, Accessed: 14 11 2021.

[34] "Bombardier Q200," https://web.archive.org/web/20161005085725/https://www2.bombardier.com/Used_Aircraft/pdf/Q200_EN.pdf, 06 2006, Accessed: 14 11 2021.

[35] "Bombardier Q300," https://web.archive.org/web/20161005085657/https:/www2.bombardier.com/Used_Aircraft/pdf/Q300_EN.pdf, 06 2006, Accessed: 14 11 2021.

[36] "Bombardier Q Series," https://web.archive.org/web/20180416074022/https://commercialaircraft.bombardier.com/content/dam/Websites/bombardiercom/supporting-documents/BA/Bombardier_Q%20Series_Final.pdf, 2017, Accessed: 14 11 2021.

[37] "Dornier 328-100 (TP)," https://328.eu/wp-content/uploads/2013/06/328-100-turboprop.pdf, 08 2013, Accessed: 14 11 2021.

[38] *Type certificate data sheet for Fokker F27*, European Aviation Safety Agency, 06 2016, issue: 06.

[39] P. Jackson, *Jane's all the World's Aircraft 2001-02*. London: Jane's Information Group, 2001.

[40] ——, *Jane's all the World's Aircraft 2003-04*. London: Jane's Information Group, 2003.

[41] "L 410 UVP-E20 Aircraft," https://web.archive.org/web/20190423024417/http://www.let.cz/files/file/KeStazeni/2016/EN_Brochure_L410_UVP-E20.pdf, 05 2016, Accessed: 14 11 2021.

[42] *Type certificate data sheet Model PA-42*, Federal Aviation Administration, 06 2010, revision: 20.

[43] *Type certificate data sheet for SD3 Series*, European Aviation Safety Agency, 06 2019, issue: 01.

[44] P. Jackson, *Jane's all the World's Aircraft 2002-03*. London: Jane's Information Group, 2002.

[45] U. S. C. on Extension to the Standard Atmosphere., *U.S. standard atmosphere, 1976 / [adopted by the United States Committee on Extension to the Standard Atmosphere]*. National Oceanic and Amospheric [sic] Administration : for sale by the Supt. of Docs., U.S. Govt. Print. Off Washington, 1976.

[46] A. D. Anderson, N. J. Renner, Y. Wang, S. Agrawal, S. Sirimanna, D. Lee, A. Banerjee, K. Haran, M. J. Starr, and J. L. Felder, "System weight comparison of electric machine topologies for electric aircraft propulsion," in *2018 AIAA/IEEE Electric Aircraft Technologies Symposium (EATS)*, 2018, pp. 1–16.

[47] A. Dubois, M. van der Geest, J. Bevirt, S. Clarke, R. J. Christie, and N. K. Borer, "Design of an electric propulsion system for sceptor," in *Aviation Technology, Integration, and Operations Conference*, no. AIAA

Paper 2016-3925. American Institute of Aeronautics and Astronautics, Jun. 2016.
[48] J. Pyrhönen, T. Jokinen, V. Hrabocová, and H. Nimelä, *Chapter 6: Main Dimensions of a Rotating Machine*, 1st ed. Wiley, 2009.
[49] X. Zhang and K. Haran, "High-specific-power electric machines for electrified transportation applications-technology options," 09 2016, pp. 1–8.
[50] R. Qu, M. Aydin, and T. Lipo, "Performance comparison of dual-rotor radial-flux and axial-flux permanent-magnet bldc machines," 07 2003, pp. 1948 – 1954 vol.3.
[51] P. B. Reddy, A. El-Refaie, K.-K. Huh, J. K. Tangudu, and T. M. Jahns, "Comparison of interior and surface PM machines equipped with fractional-slot concentrated windings for hybrid traction applications," in *2011 IEEE Energy Conversion Congress and Exposition*, 2011, pp. 2252–2259.
[52] B. Boazzo, G. Pellegrino, and A. Vagati, "Multipolar SPM machines for direct drive application: A comprehensive design approach," in *2012 IEEE International Energy Conference and Exhibition (ENERGYCON)*, 2012, pp. 98–105.
[53] H. Qiu, Y. Zhang, C. Yang, and R. Yi, "Performance analysis and comparison of PMSM with concentrated winding and distributed winding," *Archives of Electrical Engineering*, vol. 69, no. 2, p. 303–317, 2020.
[54] S. Fang, H. Liu, H. Wang, H. Yang, and H. Lin, "High power density pmsm with lightweight structure and high-performance soft magnetic alloy core," *IEEE Transactions on Applied Superconductivity*, vol. 29, no. 2, pp. 1–5, 2019.
[55] A. Krings, M. Cossale, A. Tenconi, J. Soulard, A. Cavagnino, and A. Boglietti, "Magnetic materials used in electrical machines: A comparison and selection guide for early machine design," *IEEE Industry Applications Magazine*, vol. 23, no. 6, pp. 21–28, 2017.
[56] *Soft magnetic Cobalt-Iron alloys*, Vacuumschmelze, 04 2021, vacoflux and Vacodur.
[57] *Super Core Electrical steel sheets for high-frequency application*, JFE Steel Corporation, 04 2021, jFE in-house data.
[58] P. Sekerak, V. Hrabovcova, J. Pyrhonen, L. Kalamen, P. Rafajdus, and M. Onufer, "Comparison of synchronous motors with different permanent magnet and winding types," *IEEE Transactions on Magnetics*, vol. 49, no. 3, pp. 1256–1263, 2013.
[59] HGT Advanced Magnets Co.,Ltd, "Typical Physical and Chemical Properties of Some Magnetic Materials." [Online]. Available: https://www.advancedmagnets.com/custom-magnets/
[60] *VAC Laminations & Assemblies for Motor and Generator Applications*, Vacuumschmelze, 11 2019.
[61] *Neodymium-Iron-Boron Magnet Grades Summary Product List & Reference Guide*, Arnold Magnetic Technologies, 10 2017, revision: 181031.
[62] A. I. Pressman, K. Billings, and T. Morey, *Switching Power Supply Design*, 3rd ed. New York: McGraw-Hill, 2009.
[63] *Ti 6AL-4V Datasheet*, Maher, 02 2020, revision: 01.
[64] Engineering Information, Conversions and Calculations. Shear stress and angular deflection calculator. [Accessed: 15 12 2021]. [Online]. Available: https://eicac.co.uk/Torsion-in-Shaft-Calculator
[65] T. D. Strous, "Design of a permanent magnet radial flux concentrated coil generator for a range extender application," in *Electric Energy Conversion, Delft University of Technology*, 2010.
[66] T. Burress, S. Campbell, C. Coomer, C. Ayers, A. Wereszczak, J. Cunningham, L. Marlino, L. Seiber, and H.-T. Lin, "Evaluation of the 2010 toyota prius hybrid synergy drive system," 01 2011.
[67] COMSOL AB, "Comsol multiphysics." [Online]. Available: www.comsol.com
[68] A. Krings, "Iron losses in electrical machines — influence of material properties, manufacturing processes, and inverter operation," Ph.D. dissertation, KTH School of Electrical Engineering, 04 2014.
[69] A. Lehikoinen, "Arkkio's method for torque computation," Jan 2017. [Online]. Available: https://www.anttilehikoinen.fi/research-work/arkkios-method-torque-computation/
[70] Marcusroos. (2008) Fokker 50, made in inkscape. File: File:Fokker50.svg. [Online]. Available: https://commons.wikimedia.org/wiki/File:Fokker50.svg
[71] *Type certificate for Engine - PW100 series engines*, European Aviation Safety Agency, 03 2018, issue: 04.
[72] M. Kingsley-Jones and A. Fafard, "World airliner census," accessed: 14 11 2020. [Online]. Available: https://www.flightglobal.com/download?ac=73559
[73] Airbus Defence & Space, "A400M specifications," https://web.archive.org/web/20151018162055/http://militaryaircraft-airbusds.com/Aircraft/A400M/A400MSpec.aspx, 2015, Accessed: 14 11 2021.
[74] B. Alderks, "Slot fill and design for manufacturability," 2020. [Online]. Available: https://windings.com/technical-reference/slot-fill-and-design-for-manufacturability/
[75] "Our efforts," *Mitsubishi Electric — Automotive Equipment*, Jun 2022, [Accessed: 01 06 2022]. [Online]. Available: https://www.mitsubishielectric.com/bu/automotive/our-efforts/index.html
[76] D. Ionel, M. Popescu, M. McGilp, T. Miller, S. Dellinger, and R. Heideman, "Computation of core losses in electrical machines using improved models for laminated steel," *Industry Applications, IEEE Transactions on*, vol. 43, pp. 1554 – 1564, 12 2007.
[77] M. Ghassemi, A. Barzkar, and M. Saghafi, "All-electric nasa n3-x aircraft electric power systems," *IEEE Transactions on Transportation Electrification*, pp. 1–1, 03 2022.
[78] *Dynamic Analysis of the STARC-ABL Propulsion System*, Oct 2019.

Appendix A
Figures

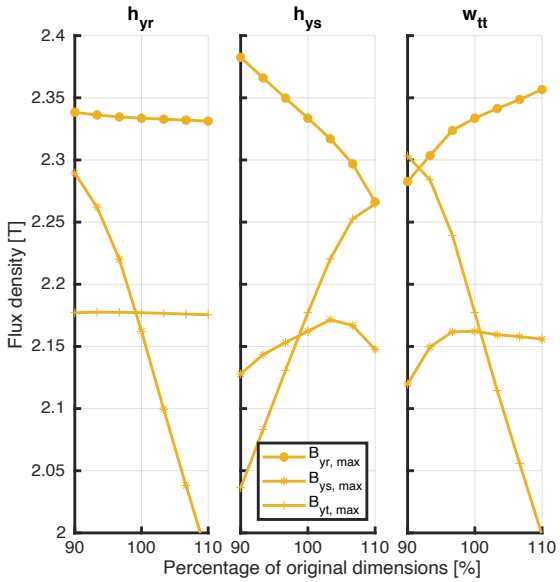

(a) $P_r = 820$ kW. No design alteration required

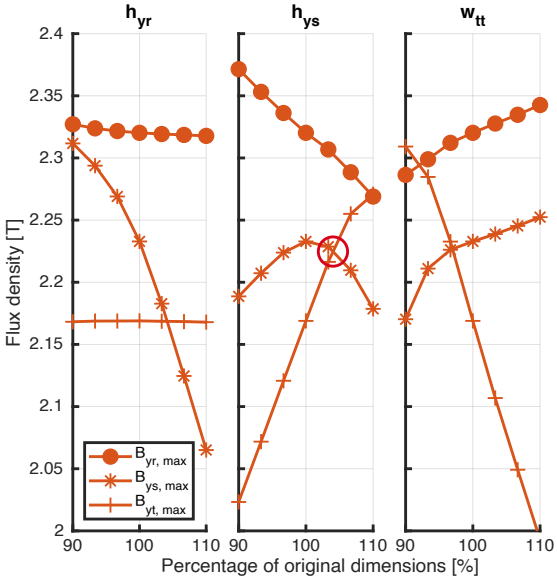

(b) $P_r = 1.8$ MW. Selected design variation is circled.

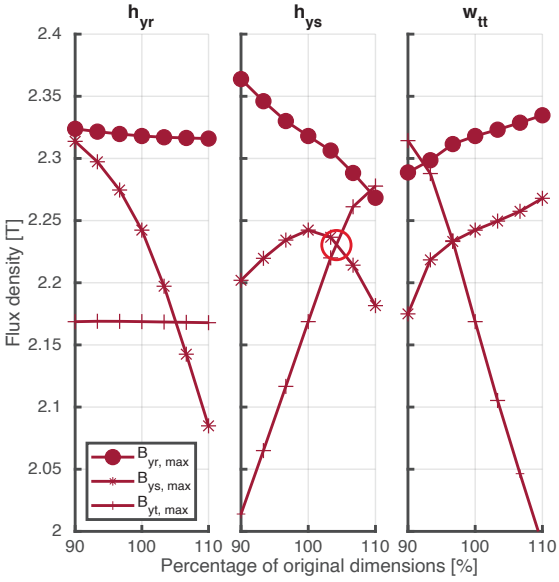

(c) $P_r = 3.0$ MW. Selected design variation is circled.

Figure 22: Results of FEM simulations. Maximum flux density in different irons as a function iron dimensions for three motors.

Appendix B
Tables

Table XX:
Output motor designs using FEM.
B) Base geometry C) Optimized h_{us} D) Optimized h_{ys}

	0.82 MW			1.8 MW			3.0 MW		
	B)	C)	D)	B)	C)	D)	B)	C)	D)
h_{ys} [mm]	12.60	12.60	—	17.80	17.80	18.50	22.50	22.50	23.42
h_{us} [mm]	41.70	36.06	—	44.70	37.92	37.29	45.70	38.83	38.28
J [A/mm]	5.546	6.468	—	5.424	6.469	6.498	5.431	6.469	6.497
Magnet mass [kg]	14.0	14.0	—	28.2	28.2	28.2	45.1	45.1	45.1
Iron mass [kg]	116.1	109.0	—	278.7	261.5	263.0	503.8	476.2	480.1
Active winding mass [kg]	35.8	30.3	—	72.1	60.0	58.9	113.1	94.5	93.0
Endwinding mass [kg]	19.7	16.7	—	39.7	33.0	32.4	62.4	51.9	51.1
Shaft mass [kg]	4.2	4.2	—	5.9	5.9	5.9	7.5	7.5	7.5
Enclosure mass [kg]	63.3	58.0	—	141.5	129.6	129.5	243.9	225.0	225.6
Total mass [kg]	253.0	232.2	—	566.1	518.2	517.8	975.5	900.1	902.3
Specific power [m^2/s^3]	3.24	3.53	—	3.18	3.47	3.48	3.06	3.33	3.32
Specific torque [Nm/kg]	21.34	23.26	—	27.60	30.15	30.18	32.10	34.78	34.70
Average power output [kW]	820	820	—	1800	1800	1800	3000	3000	3000
Efficiency	98.26	98.29	—	98.63	98.61	98.62	98.72	98.68	98.69
Maximum tooth flux [T]	2.1835	2.1771	—	2.174	2.1689	2.2247	2.1713	2.1687	2.2308
Maximum stator flux [T]	2.1582	2.1626	—	2.2346	2.2329	2.2256	2.2457	2.2424	2.232
Maximum rotor flux [T]	2.3388	2.3336	—	2.3251	2.3202	2.3042	2.3206	2.3181	2.3033
RMS coil current [A]	208.07	205.43	—	290.09	287.78	283.72	360.7	358.86	354.74
Linear current density [A/m]	4918.2	4855.8	—	4854.3	4815.6	4747.6	4783.9	4759.5	4704.8
Iron eddy current losses [W]	7595.1	6854.2	—	10458	9533.3	9518.5	13185	12281	12113
Iron hysteresis losses [W]	2025	1867.5	—	3616.9	3341.9	3365.1	5340	4983.6	4989.1
Magnet eddy current losses [W]	609.98	601.44	—	2716.2	2696.6	2679.4	7476.6	7461.4	7448.2
Coil losses [W]	4302.4	4953.9	—	8291.4	9810.3	9715.1	13029	15439	15327

Table XXI:
Base input parameters for COMSOL geometry

P_r	N_r	α_m	D_{ir}	h_{11}	h_{12}	h_{ag}	h_{us}	h_{yr}	h_{ys}	k_{fill}	l_m	w_{tt}	w_0	λ
820 kW	1450 rpm	5/6	555 mm	5 mm	5 mm	2.5 mm	41.7 mm	13.0 mm	12.6 mm	0.45	10 mm	26.9 mm	4 mm	0.2
1800 kW	1100 rpm	5/6	795 mm	5 mm	5 mm	2.5 mm	44.7 mm	18.0 mm	17.8 mm	0.45	10 mm	38.0 mm	4 mm	0.2
3000 kW	915 rpm	5/6	1010 mm	5 mm	5 mm	2.5 mm	45.7 mm	22.5 mm	22.5 mm	0.45	10 mm	48.0 mm	4 mm	0.2